# EPRG-PRCI-APGA
# 23rd Joint Technical Meeting
# Edinburgh, Scotland
# 6–10 June 2022

# APPRAISAL OF THE MICROGROOVING PHENOMENON OCCURRING IN A SOUR ENVIRONMENT ON 4PB SPECIMENS

Christophe Mendibide*
French Corrosion Institute, Part of RISE, Fraisses, France

Flavien Vucko
French Corrosion Institute, Part of RISE, Brest, France

Pascaline Fourny
French Corrosion Institute, Part of RISE, Fraisses, France

* presenting author

## ABSTRACT

The formation of grooves can be observed on carbon steel specimens submitted to Sulfide Stress Cracking (SSC) tests under conditions simulating sour service. According to existing guidelines, for un-failed specimens, the presence of cracks deeper than 100 µm (EFC 16) or 500 µm (BS 8701, characterized as cracking not pitting) on the cross-section would be unacceptable and thus the steel would be rejected. However, grooves could reach such a threshold without clear evidence of cracking. The aim of this study was to gather experimental data to address the groove criticality and conditions necessary for their formation in order to propose clear recommendations on how to consider grooving.

Two different X65 grades, TMCP seamwelded steel and seamless steel, were submitted to SSC tests at 3 different levels (72, 80 and 90%AYS). The presence of micro-grooving was systematically observed under the investigated conditions, but without clear evidence of cracking. The roughness and the surface residual stresses seemed to affect the groove formation, in particular former machining marks. The applied stress showed mirror impact in the investigated range. A stress or hydrogen enhanced corrosion rate may occur at the groove tip, related to the mechanical characteristics and microstructure of the steel.

The numerical calculations showed a clear interaction of the stress fields around the groove tips, leading to stress relaxation phenomenon when the groove distance was decreased below 300 µm. For two different hardening rates (linked to YS/UTS ratio), it was exhibited that the stress concentration and the maximum hydrostatic stress close to the groove tip were affected. As a result, the local corrosion rate at the tip of the groove could be enhanced for steels with lower YS/UTS ratio, showing both higher maximum stress concentration and maximum hydrostatic stress.

## DISCLAIMER

# 1. BACKGROUND AND OBJECTIVES

The sulfide stress cracking (SSC) resistance of carbon steels and other alloys is commonly addressed through testing according to NACE TM0177, NACE TM0316 or EFC16. The Method A of the first standard is focusing on tests using uniaxial tensile (UT) while the second standard considers 4-point bend (4PB) type of loads. A common way of qualifying a material according to these standards is the absence of failure of the specimens or SSC crack initiation at the surface of the material after a test duration of 720 hours (1 month).

However, after cross-sectional observations of non-broken carbon steel specimens, superficial so-called "grooves" are often observed that can be significantly different in shape and depth depending on the material and test conditions considered. Some examples of such grooves observed after SSC tests performed at the FCI are presented in Figure 1. In some conditions, only grooves with a depth lower than 100 µm are observed (Figure 1a and b) while crack initiation at the groove tip can sometimes be highlighted (Figure 1c and d).

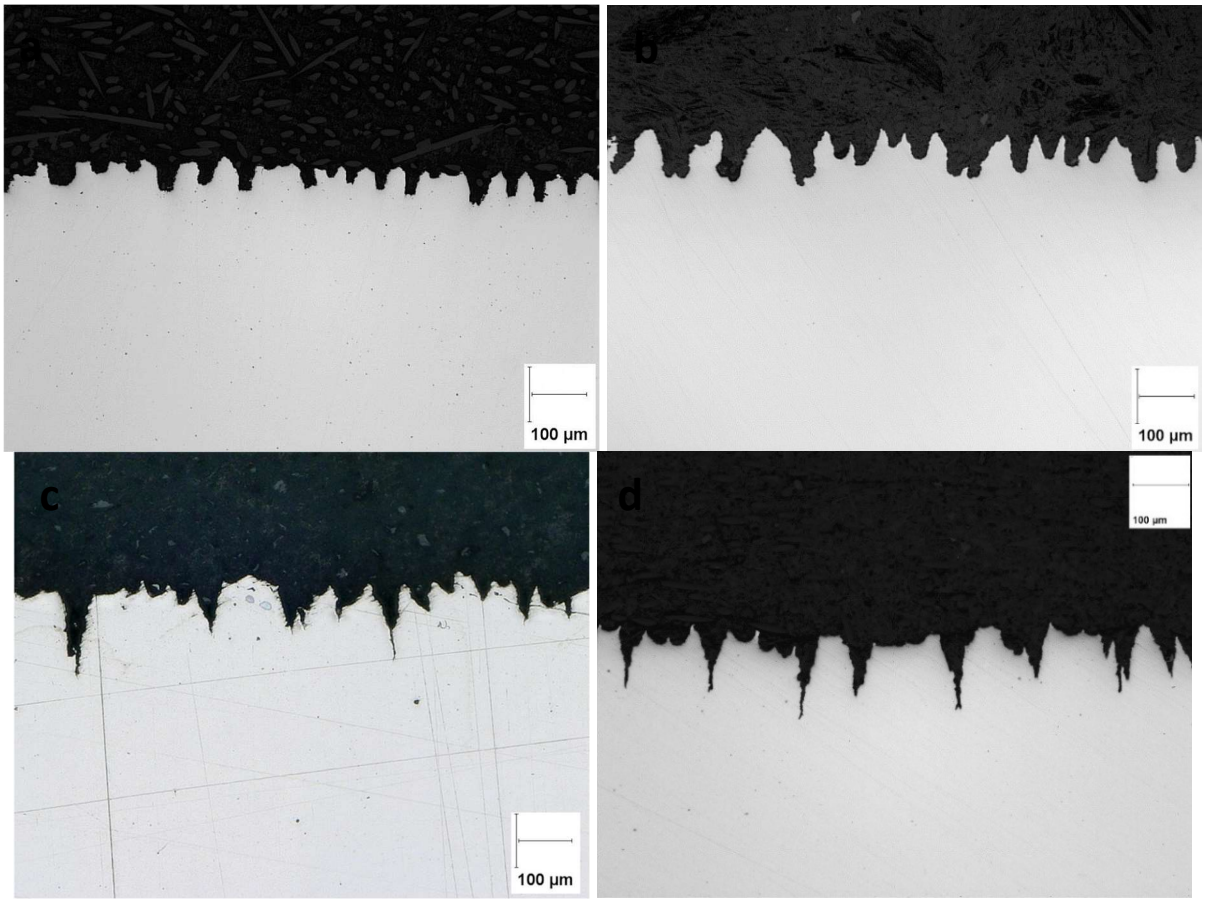


Figure 1: Example of groove observed in cross-section after sour tests performed at FCI.

In case of presence of grooves without any clear evidence of crack, it is sometimes difficult to consider the alloy "unacceptable" since the European Federation of Corrosion (EFC) indeed specifies, in the document EFC16, that any stress corrosion cracks extending more than 100 µm in the through-thickness direction should be considered as a cause of failure. Grooving with maximum depth lower than 100 µm should thus be acceptable. However, grooves observed on non-broken specimens after SSC tests can also reach this threshold depth without crack initiation and a strict application of EFC16 recommendations should thus lead to sometimes consider the presence of grooves without crack evidence as non-acceptable. No specification regarding the groove shape is specified in EFC16. On the other hand, BS 8701 accepts SSC cracks, and consequently grooves, up to 0.5 mm in depth in full ring tests.

A first approach for grooving classification was proposed by Pargeter [1]. The authors suggested distinguishing grooves criticality according to their shapes by classifying grooves, through a flow chart methodology, as “pits” (not critical) or “cracks” (critical). “Cracks” are defined as “parallel sided and sharp” indications. Even if not clearly stated by the author, the methodology suggests that sharp grooves are critical for a depth higher than 125 µm. In a recent communication from Anderson et al [2], a first industrial attempt was made for the classification of the grooves between “critical cracks” or “critical stress grooves” and “non-critical pits”. The authors discussed an empirical methodology to classify the criticality of the different patterns but the scientific data supporting this classification were not given in the paper.

In papers published by Crolet [3,4] the criticality of grooves was addressed through fracture mechanics based on data published in the literature. According to this author, grooves should be considered as “crack nuclei” that did not propagate due to stress relaxation after initiation and blunting of the crack tip with corrosion products. The author indicates that the equidistance of grooves generates a relaxation of stress below the threshold necessary to allow the propagation. Blunting of the crack tips generates a confined zone at the tip leading to a local pH decrease and thus an increase of the local corrosion rate and smoothening of the tip rendering impossible any further propagation. According to these explanations, grooves are a “false pass” and are thus unacceptable. From a work conducted by Haase et al.[5], H2S is needed to promote groove formation (no grooves are forming after testing under pure CO2) on pipeline steels, but the groove depth and shape criticality does not evolve proportionally to the H2S partial pressure. In the environments selected by the authors, almost no grooves were observed after test under 1 bar H2S while deep and sharp grooves were evidenced after experiments under 0.03 or 0.2 bar H2S (balance CO2). These results suggest either that grooving is not SSC or that there is a strong effect of scaling. In a recent paper by Mendibide et al [6], the parameters influencing the groove formation on casing steels were evaluated after sour testing under uniaxial tensile test and 1 bar H2S. The conclusion was that, in that case, grooving is not SSC but a stress assisted corrosion phenomena promoted by hydrogen uptake. Several experimental facts support this conclusion.

According to our experience, when no crack is observed through cross-sectional observations, grooves, if evidenced, are most often confined in the first 100 or 200 µm of depth below the surface. One can thus wonder if the initial surface preparation and associated roughness, residual stress or cold work, may affect the grooves generation. The beneficial effect of electropolishing on the SSC resistance of low-alloyed carbon steel has indeed already been reported [7,8]. It was also demonstrated that residual stress and cold-work, when present at the specimen surface, are located in the first tens of micrometers below the surface [9]. For very corrosive environments, leading to high corrosion rates and dissolution of the superficial layer in the first hours of immersion, it can thus be anticipated that, during standard SSC tests according to NACE TM0177, residual stress and cold-work can only affect the groove/cracks initiation but probably not the propagation. However, for lower corrosion rate, the effect of residual stress and cold-work could be more important.

It is thus important to gather experimental data to address the groove criticality and conditions necessary for their formation in order to propose clear recommendations on how to consider grooving.

## 2. MATERIAL SELECTED FOR THE STUDY

Two different materials were provided to the FCI:

- X65 - TMCP processing route / seamwelded
- X65 - seamless quenched and temper process

The tensile properties and hardness of the alloys are given in Table 1 and Table 2 respectively. The tensile tests were performed from specimens sampled in the longitudinal direction of the supplied

materials. Tensile reports are available in Appendix 1. If there is no significant difference in the hardness of both grades, the ultimate tensile strength of the seamless grade is slightly higher leading to a lower YS/UTS ratio. Both grades have an acceptable hardness for sour service according to ISO 15156.

Table 1- Mechanical properties- tensile tests

| Grade | YS (MPa) | UTS (MPa) | YS/UTS | A (%) | Z (%) |
|---|---|---|---|---|---|
| Seamwelded | 536 | 556 | 0.96 | 26 | 85 |
| | 522 | 566 | 0.92 | 28 | 85 |
| Seamless | 522 | 613 | 0.85 | 28.5 | 82 |
| | 502 | 599 | 0.84 | 24.5 | 82 |

Table 2- Hardness measurements

| Grade | Microhardness | | Macrohardness | |
|---|---|---|---|---|
| | $HV_{0.3kg}$ | Average | $HV_{30kg}$ | Average |
| Seamwelded | 206-203-204 | 204 | 193-194-190 | 192 |
| Seamless | 204-198-197 | 200 | 198-198-199 | 198 |

Figure 2 displays the microstructures of both grades observed after Nital etching. These observations were conducted on the specimens sampled for SSC testing and therefore close to the inner surface of supplied pipes.

The TMCP-seamwelded grade has structure that is mostly ferritic with presence of pearlite at grain boundaries while the seamless heat is bainitic. It is noticeable that although both grades have a different microstructure, the mechanical properties are similar.

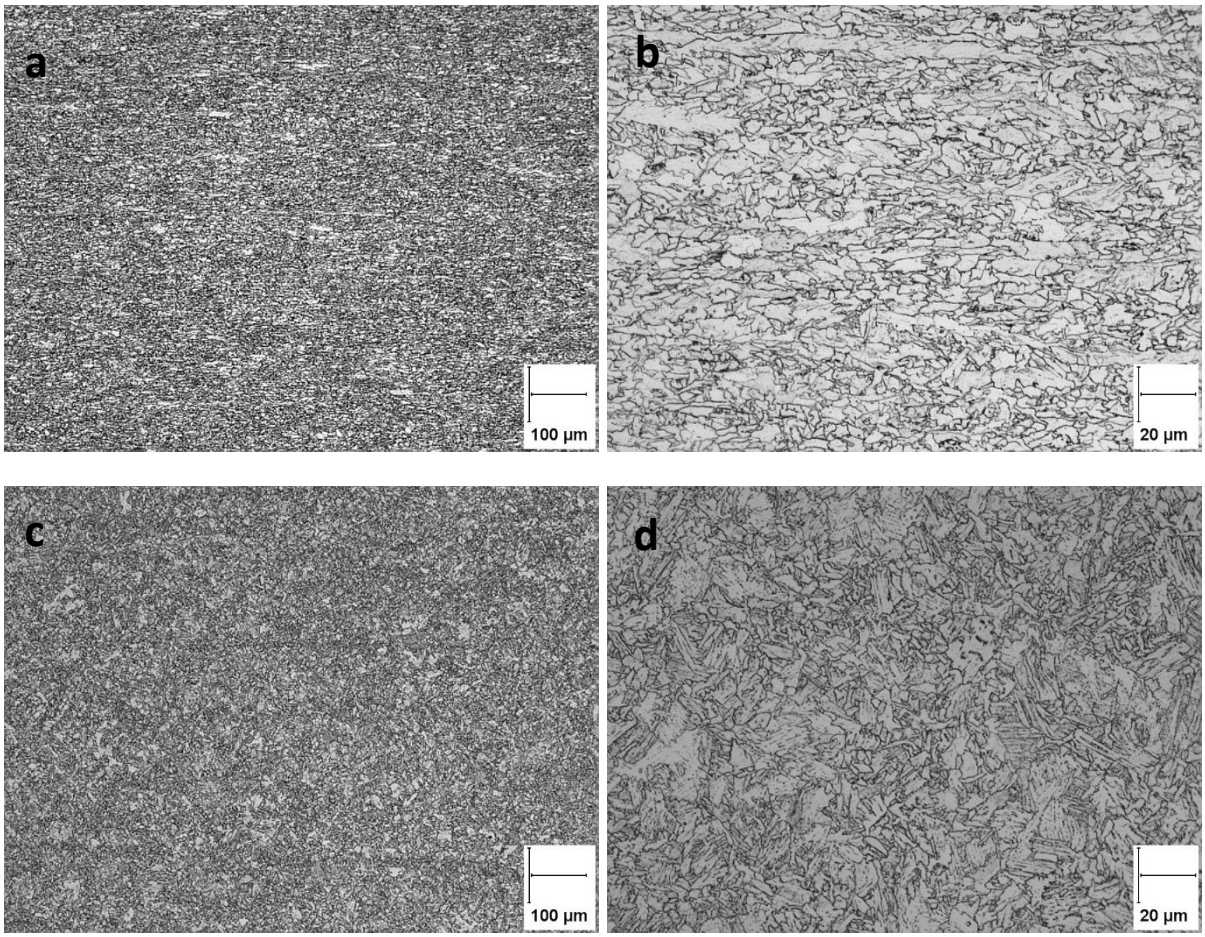

Figure 2: Microstructure of X65 materials (a-b) seamwelded TMCP (c-d) seamless

# 3. EXPERIMENTAL PROCEDURES

## 3.1. X-RA DIFFRACTION AND ROUGHNESS

Before exposure, one specimen of each test triplicate was analyzed by X-Ray diffraction to evaluate the surface residual stress using the $\sin^2 \psi$ methodology. This method consists in using the (hkl) diffraction plans as strain gauges. To achieve such measurement, the effect on the variation of the angle $\psi$ on the position of the diffraction peaks is evaluated. As presented in Figure 3, this parameter is defined as the angle of measurement between the normal to the surface of the sample and the normal to the (hkl) diffracting plane

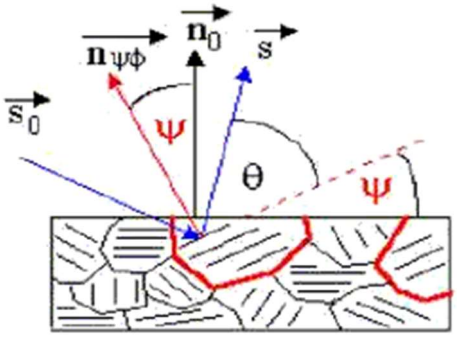

Figure 3 : Schematic presentation of the parameter $\psi$.and $\theta$ considered in the XRD analysis

If the tested sample is submitted to superficial residual stress, the lattice parameter may vary and the position (dψ) of the diffraction peak for the angle ψ is shifted versus the expected position (dn) for a residual stress-free material. (dψ) is then correlated to sin² ψ according to the following equation:

$$\varepsilon = \frac{d_{\psi -} d_n}{d_n} = \frac{1-\nu}{E}.sin^2\psi.\sigma_r \qquad (2)$$

With :

- $d_\psi$ the position of the considered diffraction peak for the angle ψ
- $d_n$ the theoretical position of the peak
- ν the poisson coefficient of the material
- E the Young's modulus of the material
- $\sigma_r$ the residual stress

By plotting ε versus sin² ψ, a line is obtained which slope is proportional to the residual stress.

All measurements were performed using the chromium radiation (λ=2.29 Angstroms) under 20 kV and 2 mA. The angle ψ was varied (13 different points per measurement) between -37° and 39° and the measurement of residual stress was performed using a peak with the theorical 2θ(dψ)=156°.

The considered Young's modulus and Poisson's coefficient were 210 GPa and 0.3 respectively

Cold-work present at the surface of different tested specimens was also estimated using the Full-Width at Half Maximum (FWHM) as schematically presented in Figure 4. Provided the use of the same X-Ray source, the relative value of this parameter for different surface preparation indeed allows to evaluate if more residual cold work is present after a given surface preparation compared to another (The higher this parameter and the higher the cold-work). One residual stress profile was also established by XRD. This technique being destructive, a dedicated specimen was used for the measurement.

The superficial XRD measurements were conducted on both materials for each surface state. The surface state "P1200" was selected to assess the residual stress profile in the skin of the material. Only the seamwelded grade was used for the stress profile evaluation. To build these stress profiles, a superficial layer in the area of measurement was locally dissolved using electrolytic etching before each measurement.

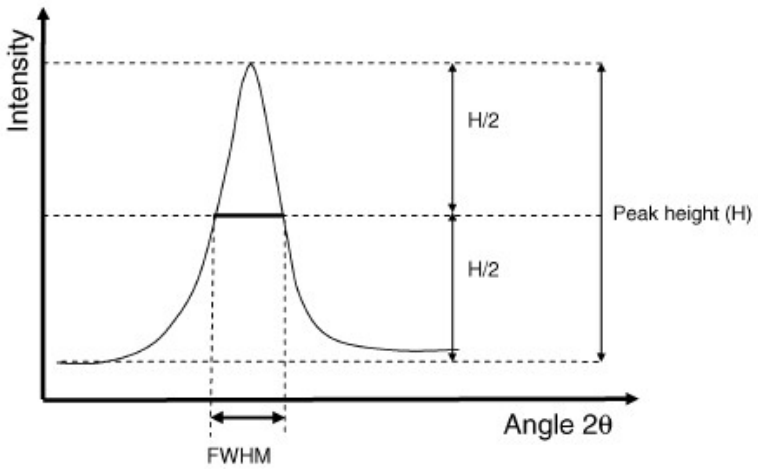

Figure 4 : Schematic presentation of FWHM

Roughness measurements were also completed after each surface preparation (as-machined, P80, P1200, Mirror finish) using optical profilometry.

## 3.2. MODELLING

The numerical calculations were performed by finite elements modelling using continuum mechanics. The geometry was built in 2D, assuming plane strain condition representative of 4PB samples. The characteristics of the grooves were parametrized in terms of depth, width and distribution (distance between 2 successive grooves). The properties of the steel were based on uniaxial tensile test. The boundary conditions were set to mimic 4PB keeping the outer surface at 90%AYS. Finally, the mesh was refined to decrease the calculations error.

### *3.2.1.* GEOMETRY

4PB specimens consisted in plates of 140 mm long, 15 mm large and 5 mm thick. For the simulation, a 2D model was used with plane strain assumption that simulate thick sample. Then, thanks to the symmetry of the sample, only one half of the sample was drawn, as shown in Figure 5. The length was also reduced to 60 mm (instead of 70 mm) as the length out of the loading points was not relevant for the evaluation of the stress distribution. Additional domains were defined to allow the addition of microgrooves and application of the boundary conditions.

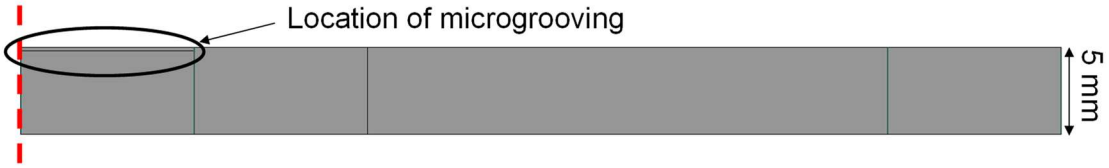


Figure 5: Geometry of the 4PB sample. The axial symmetry is indicated by a red dash line.

V-shape microgrooves were considered in this study. However, real V notch cannot be modelled by FEM as resulting in a singularity. Thus, a small radius of 1 µm was drawn at the tip of the groove. Under such conditions, the minimum width of the notch was 2 µm. The other characteristics of the microgrooves are summarized in Table 3 and illustrated in Figure 6. The groove distribution corresponded to the distance between the edge of two successive grooves, so that the width should be added to calculate the distance between two microgroove centers.

Table 3: Characteristics of the microgrooves

| Parameter | Min | Mid | Max |
|---|---|---|---|
| L - Groove depth (µm) | 50 | 100 | 500 |
| W - Groove width (µm) | 2 | 10 | 20 |
| D - Groove distribution (µm) | 10 | 100 | 500 |

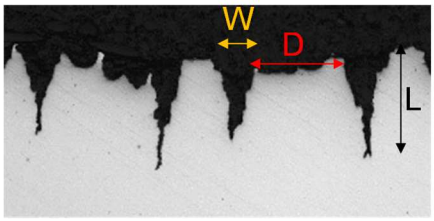


Figure 6: Characteristics of microgrooves.

Examples of modelled microgrooves are given in Figure 7. In all cases, rather sharp grooves were obtained that could lead to severe stress concentration factors (theoretically from 16 to 50 [10]) at the groove tip when considered individually. However, interaction of the stress fields between grooves should contribute to decrease the apparent stress concentration factor.

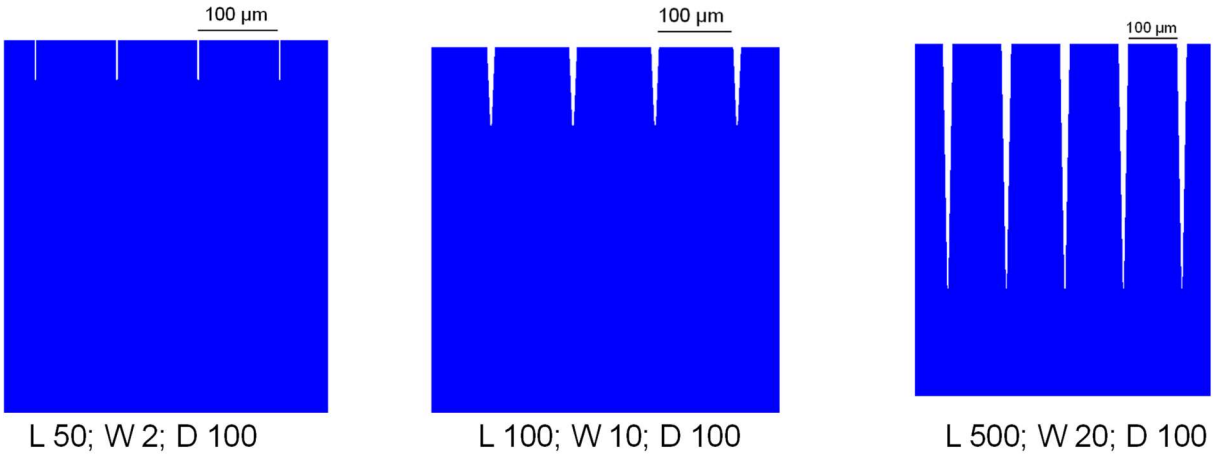


Figure 7: Examples of microgrooves in the numerical model (L=length in µm, W=width in µm and D=distance between 2 grooves in µm).

### *3.2.2.* MECHANICAL PROPERTIES

For the simulation, the mechanical properties of the steel were directly extracted from the experimental uniaxial tensile curve presented in Figure 8. This curve was close to the type of curve obtained for the TMCP seamwelded steel, showing a UTS at around 560 MPa. For the comparison, some calculations were also performed using a higher UTS (600 MPa) corresponding to the seamless steel.

In the model, the true stress-strain curve was necessary. Such data were calculated from the engineering stress-strain curve using the following equations:

$$\varepsilon = ln(1 + \varepsilon_n) \quad \text{(x)}$$

$$\sigma = \sigma_n \times (1 + \varepsilon_n) \quad \text{(x)}$$

with $\sigma$ and $\varepsilon$ the true stress and strain and $\sigma_n$ and $\varepsilon_n$ the engineering stress and strain.

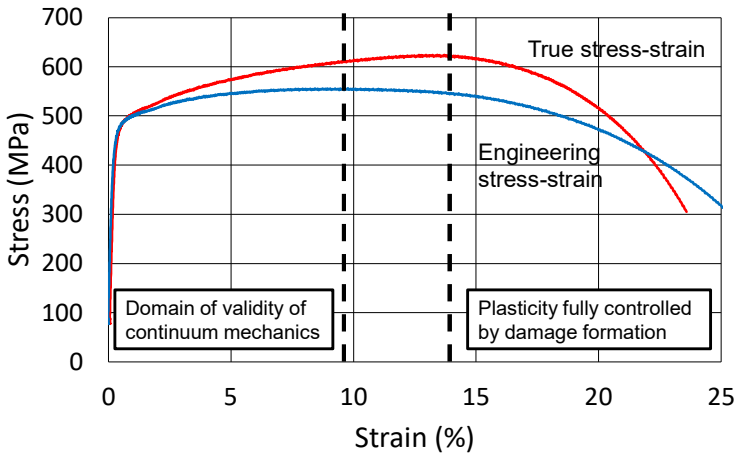


Figure 8: Uniaxial tensile curve for X65 steel in engineering stress-strain and true stress-strain.

Models of continuum mechanics are valid when the plasticity is controlled by dislocations nucleation/annihilation and mobility mechanisms. For large plastic deformation, ductile damage can initiate (voids nucleation and coalescence) and the plasticity becomes fully controlled by mechanisms of damage formation [11]. Thus, the calculations performed in this study would be valid up to the maximum tensile strength of the steel as ductile damage should initiate for higher stresses, significantly modifying the local strain and stress distribution.

For the simulation, an idealized curve was implemented (smoothed) extrapolated up to 650 MPa for very large deformation (100%).

### *3.2.3.* BOUNDARY CONDUITIONS

The specimens were tested under 4-points bending. As shown in Figure 9, the distance between the two inner loading points was 40 mm and 100 mm for the 2 outer supporting points. In the model, as only half of the sample was drawn, the loading point was at 20 mm from the axial symmetry line and the supporting point at 50 mm.

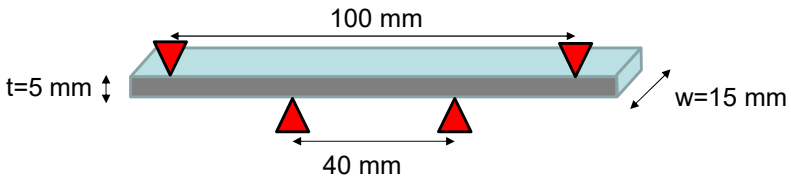


Figure 9: Sketch of 4PB specimen

To evaluate the required displacement that should be applied on the loading point to reach 90%AYS on the surface, a numerical calculation without microgrooves in the gauge section was performed. The maximum stress on the outer surface was evaluated as a function of the imposed displacement. As shown in Figure 10, a displacement of 1.03 mm was necessary to reach the required stress. The same displacement was imposed in the case of geometries with microgrooves.

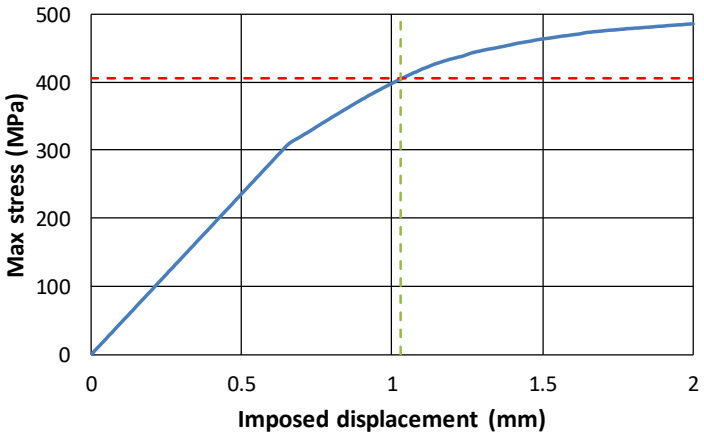


Figure 10: Calculation of the maximum stress as a function of imposed displacement on the load point.

### 3.2.4. MESHING

The size of the mesh can have a strong impact on the results of the FEM calculations. Thus, additional surfaces close to the tip of the notch was drawn (see Figure 11) to adapt a refined mesh at this location.

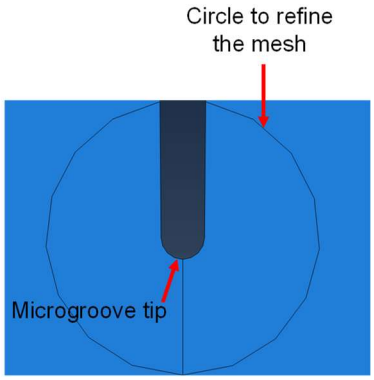


Figure 11: Detail of the microgroove tip with additional circle to apply mesh refinement.

To evaluate the required size of the mesh close to the microgroove tip that would limit the calculation errors, simulations were performed for different mesh sizes. As presented in Figure 12, the mesh should be refined down to 0.2 µm to limit the error below 1 MPa. Such a dimension was selected for all the calculations performed in this study.

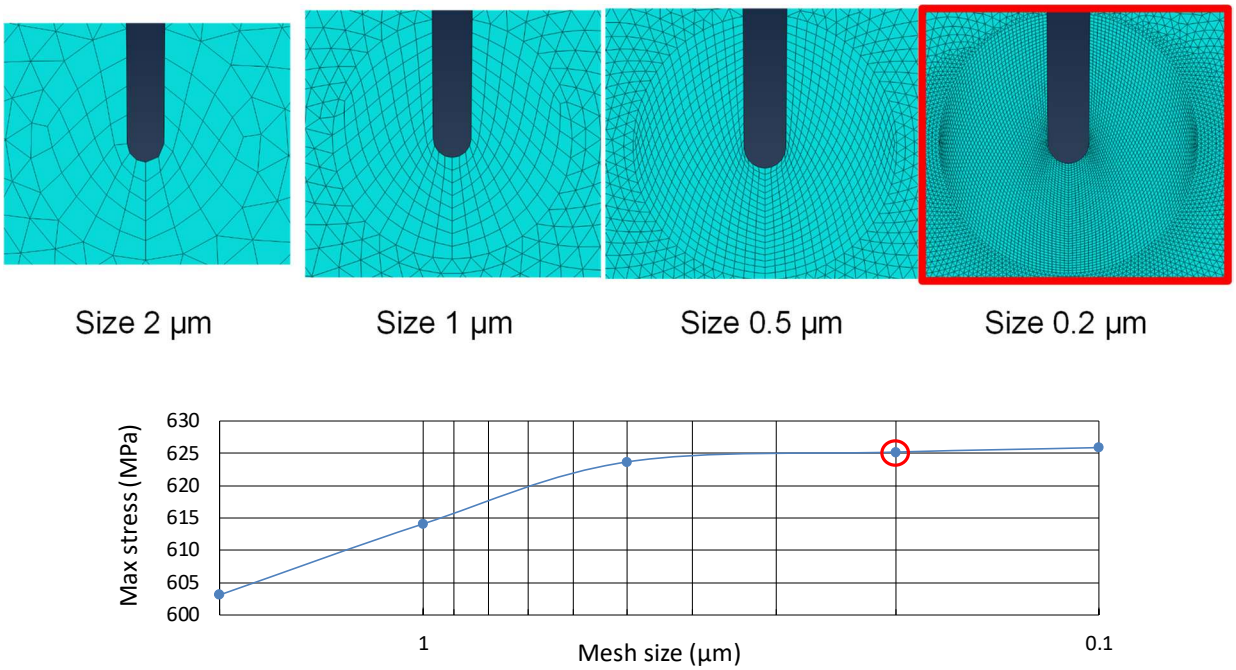


Figure 12: Examples of refined mesh close to the groove tip and evaluation of the maximum stress for the same boundary conditions.

### *3.2.5.* VALIDATION OF THE MODEL

The objective of the study was to evaluate the stress relaxation effect linked to the interaction of several grooves at the surface of 4PB specimens. For the same boundary conditions, calculations were done with 10, 15 and 20 grooves (L=500µm, W=10 µm and D=100µm) close to the symmetry axis, representing 19 to 39 grooves. As shown in Figure 13 and Figure 14, the stress field was different the closer to the last groove, far from the center of the specimen, that clearly showed over-stresses. Out of the 7 last grooves, the stress distribution at the tip of the grooves was rather similar.

Considering the maximum stress at the location of the 4th groove from the center, a slight deviation of 3 MPa was observed in the case of the modelling with 10 grooves (628.4 MPa) compared to the 2 other cases (625.2 MPa). Thus, at least 15 grooves should be modelled to avoid edge effects.

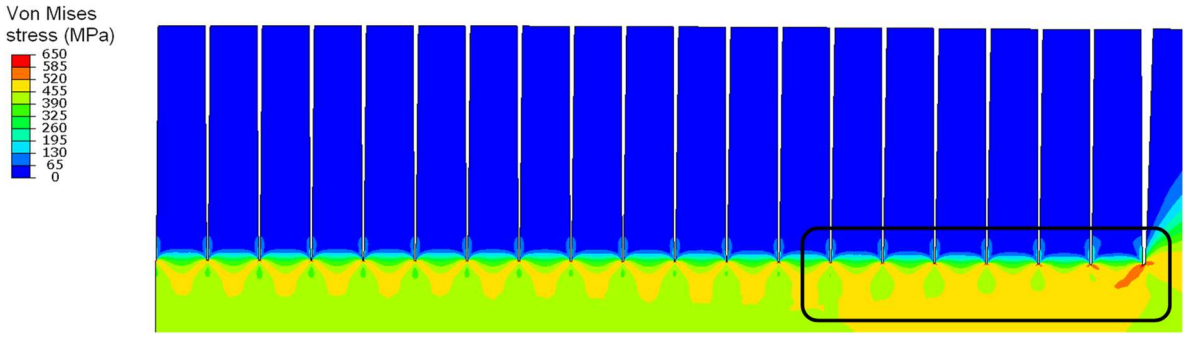


Figure 13: Stress distribution calculated with 20 grooves.

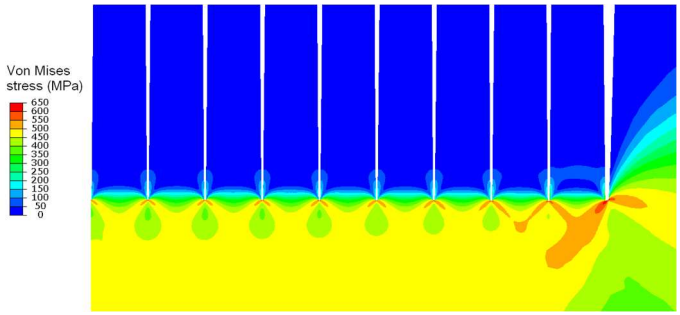


Figure 14: Stress distribution calculated with 10 grooves.

It should be pointed out that using 500 µm deep microgrooves, the stress at the tip of the grooves was rather high, very probably out of the domain of validity of the model. Thus, damage or even cracking should be expected under such conditions.

## 3.3. SSC TESTS

### *3.3.1.* SSC TESTS CONDITIONS

The standard geometry of the 4PB specimens was 140x15x5 mm3, prepared by milling ensuring that no more than 0.25 µm of material was removed in the two last machining passes. Before delivery, the specimens are roughly ground at the machining shop to achieve a final average roughness lower than 0.8 µm.

From delivery, in standard test conditions, all parts are then polished down to grit paper P1200 before SSC test. The polishing is performed using 5 intermediate grit papers from P80 to P1200 and the last polishing step is completed in the longitudinal direction of the specimens. However, to evaluate the effect of the initial surface state as requested by EPRG, three other final surface finish were studied:

- As machined
- P80
- Mirror finish using a diamond past as final polishing step.

The 4PB specimens were loaded using common loading jigs immersed in the vessel containing the test solution. The load was applied using strain gauges positioned in the middle of each specimen and removed before exposure using acetone.

A schematic presentation of the test vessel is given in Figure 15

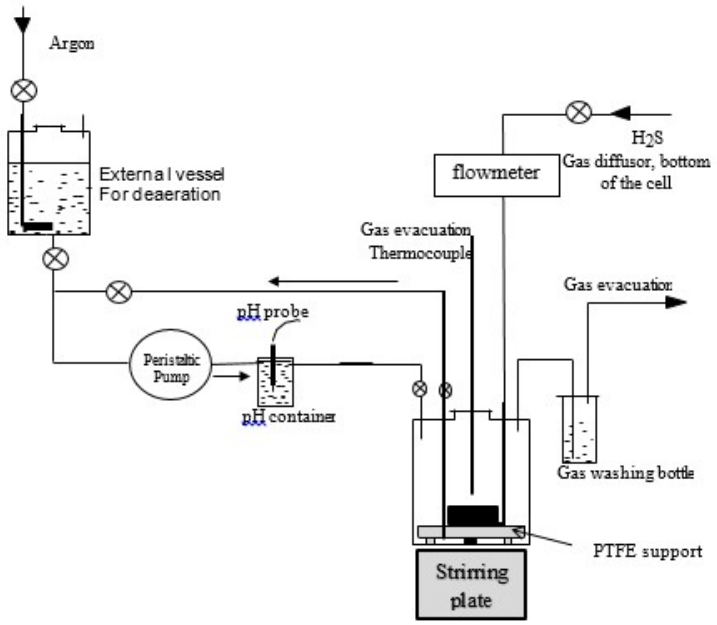


Figure 15 : Schematic presentation of the test vessel for 4PB tests

The test environment selected for the program was NACE TM0177 Solution A. The composition of this standard solution is 5%wt NaCl + 0.5% wt acetic acid with demineralized water. The solution was prepared using demineralized water of controlled conductivity (<5 µS.cm-1) and analytical grade products. The initial pH was 2.6-2.8. The pH was monitored but not controlled during the test.

The H2S partial pressure was 1 bar and achieved by saturating the solution with pure H2S at atmospheric pressure. The test temperature was 24±3°C and the test duration 720 hours.

The 4PB experiments were conducted according to NACE TM0316. The deformation applied to the specimens to achieve the targeted tensile stress (72, 80 or 90%AYS) was controlled using strain gauges positioned on the surface submitted to the tensile stress during the test and removed with acetone before exposure. The level of strain was defined using the mechanical test results (The Stress-Strain plots given in appendix). The standard 4-PB holders used at FCI have a length between the outer roller of 100 mm and 40 mm between the inner. The volume to surface ratio (V/S) was 50 mL/cm2 in all experiments.

The tests were carried out in a glass cell. After introduction of the 4-PB specimen, a deaeration of the vessel was performed by argon bubbling during a few hours. The solution was deaerated separately. The solution was then pushed in the cell with the inert gas, and the deaeration was completed by keeping the Argon bubbling in the vessel. The oxygen level was measured using an oxygen probe. Deaeration was continued until dissolved oxygen was below 10 ppb.

Once this threshold was reached, argon bubbling was stopped and saturation with H2S gas was performed during two hours at a high flow rate (~200 mL/min). To check the saturation of the solution, the sulfide content was measured using iodometric titration. If the minimum sulfide content specified by NACE TM0177 was reached (2300 ppm minimum but the actual level was always higher – 3200 ppm maximum can indeed be reached according to the Henry's law), the gas flow rate was reduced and maintained at a lower flow rate (~20 mL/min). The initial pH was measured at the same time. Testing was performed in pH-free conditions and the pH evolution was nevertheless monitored during the whole duration of the immersion. The temperature was measured using a thermocouple in a glass finger located inside the solution. It was also monitored during the whole test.

When the test was completed, argon was bubbled before opening to desaturate the solution. The specimens were then rinsed and brushed with tap water. They were stripped in an ultrasonic bath containing inhibited hydrochloric acid. After cleaning, they were rinsed with water, then acetone and dried with cool air.

The load levels requested by EPRG were 72, 80 and 90% AYS. These different applied stresses were only considered with the P1200 surface finish. The effect of surface preparation (as-machined, P80, P1200, Mirror) was only evaluated under a stress of 90% AYS.

After test, all specimens were checked by magnetic particle inspection (MPI) to highlight possible crack initiation before to characterize the microgrooving though metallographic observations

### *3.3.2.* MICROGROOVING CHARACTERIZATIONS

The evaluation of the groove distribution was performed using numerical microscopy (Keyence tradename) and an example of measurement is presented in Figure 16. The surface scales present on the specimens after exposures were dissolved using hydrochloric acid inhibited with hexamethylenetetramine as per ASTM G1. Then, from a metallographic cross-section, the grooves are first assigned colors from which their dimensions (depth (d) and width (w)) were automatically determined by image analysis. The groove depth and shape factor (the ratio d/w) of each groove was then estimated. Grooves with a high shape factor are sharp and thus could possibly be cracks while those with a low shape factor are smooth. The groove depths are measured with respect to a base line at the top of the grooves (the surface). The position of the baseline is not corrected for corrosion considering that the average corrosion rate and associated impact on the baseline are the same for all materials.

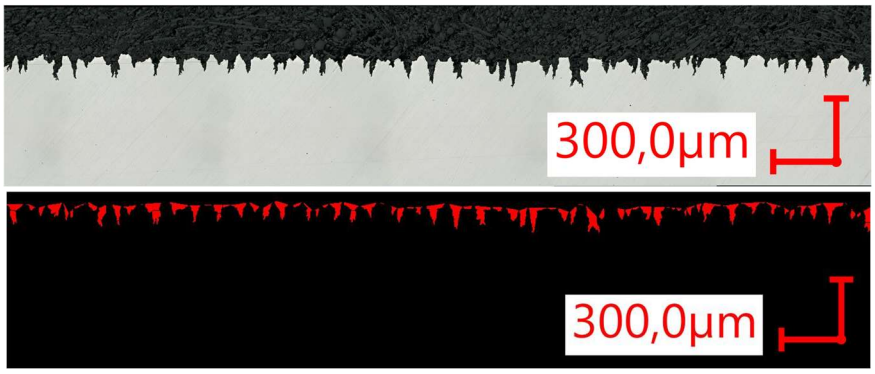


***Figure 16:*** *Example of groove dimension measurement by image analysis*

This analytical approach offers a statistically significant number of measurements since several hundreds of measurements per specimen can be obtained. The statistical distribution of the groove depth can then be plotted and compared for the different test conditions considered in the program.

To conduct a statistical analysis of the groove depth, the probability for each groove to reach a given threshold is determined. For example, the depth of each groove is first measured, and the measurements then ranked in an ascending order. We then define the probability as “P=i/n” where “i” is the measurement number and “n” the total number of measurements performed. Plotting P versus the measured parameter leads then to the results presented in Figure 17. For the shape factor, only the values higher than 1 are considered lead to only select the “sharp” grooves (those having a depth higher

than their width) leading to possible high stress concentration at groove tip. In the example presented, 20% of the measured depths were greater than 50 µm and the maximum depth measured was 160 µm. Also, 5% of the grooves had a shape factor higher than 2.

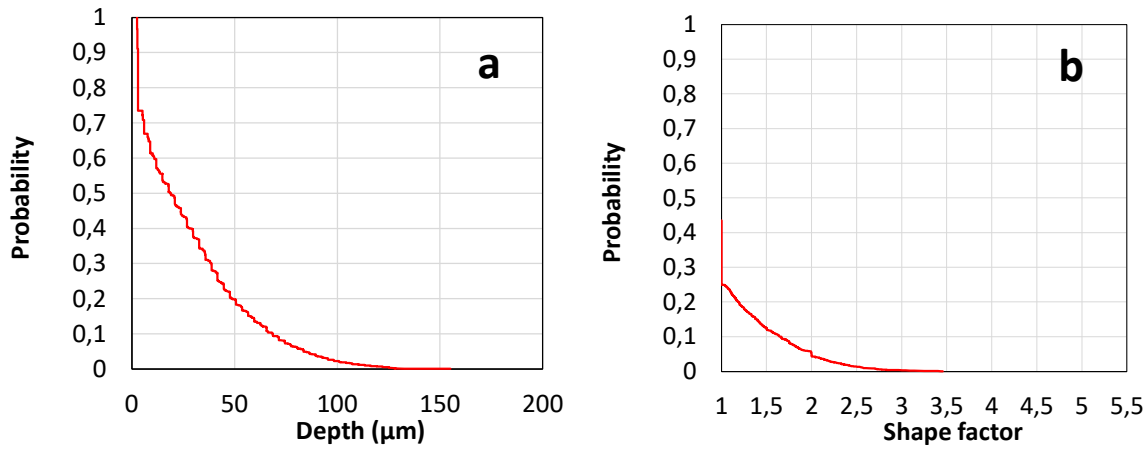


Figure 17: Example of probability versus depth of the different grooves measured through cross-sectional observations. Measurements using image analysis. 2610 measurements.

# 4. RESULTS

## 4.1. MODELLING

### *4.1.1.* PARAMETRIC STUDY

The stress and strain fields were evaluated for the cases presented previously in Table 3 i.e. 27 different calculations. Moreover, reference cases were modelled with a single groove in the gauge section of the 4PB sample. An example in the case of 50 µm deep, 2 µm wide and a distribution of 10 µm is shown in Figure 18. The maximum stress concentration at the tip of the single groove reached 639.1 MPa (out of the domain of validity of the model – ductile damage can be expected), whereas the max. stress remained at 534 MPa with a close-packed groove distribution. Thus, a strong stress relaxation was obtained due to the interaction of the stress fields around the grooves.

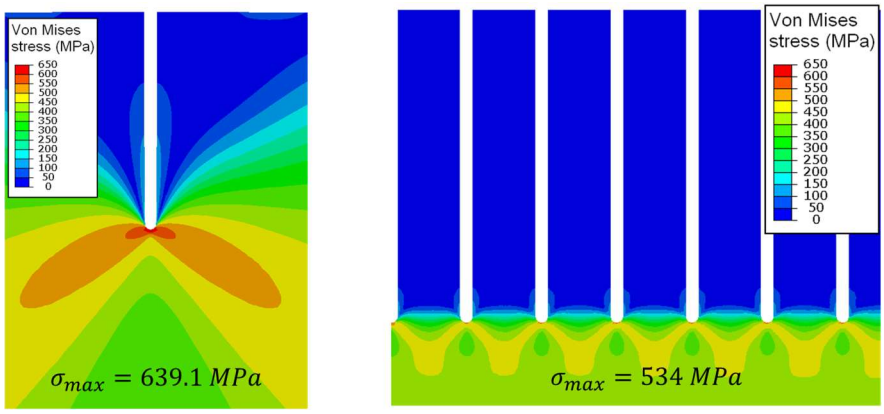


Figure 18: Numerical calculation of the stress distribution for (left) one single groove and (right) several grooves on the 4PB sample. L=50µm, W=2µm, D=10 µm.

For each case, the maximum stress at the groove tip is reported as a function of the distance between 2 groove centers in Figure 19. With increasing distance, the maximum stress tended to the value

calculated with a single groove. For a distance higher than 300 µm, the interaction between grooves could be neglected.

In the range of distance from 10 µm to 150 µm, it could be observed that for groove depth of 50 and 100 µm the maximum stresses were in the same range, the distance being the main controlling factor. For deeper groove, i.e. 500 µm, the maximum stress was clearly higher in the range of investigated distances. Each set of 3 points closely packed corresponded to the 3 different widths used in the calculation. Thus, it could be observed that the width of the groove, in the range of 2 to 20 µm, did not significantly influence the results. Indeed, considering the theoretical calculations of the stress concentration at the tip of a notch, the most important parameters are the depth of the notch and the radius at the notch tip.

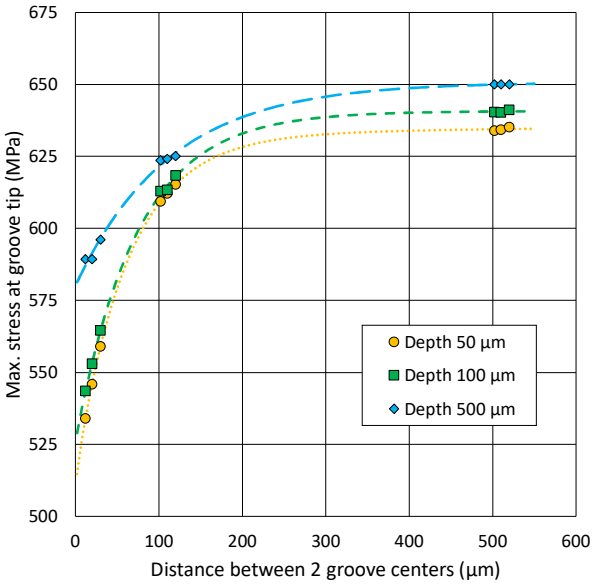


Figure 19: Evolution of the maximum stress at the tip of the grooves as a function of the groove distance and depth.

A clear stress relaxation could be observed when several grooves were distributed over the surface of the 4PB samples. But, to assess the risk of hydrogen assisted cracking at the tip of the grooves, other mechanical factors should be investigated: the plastic deformation and the hydrostatic stress. The plastic deformation, strongly linked to dislocations, can increase the local amount of trapping sites and consequently the local concentration of hydrogen. Moreover, plastic deformation may play a role on the corrosion mechanism of the steel, which could favor the local anodic dissolution. Hydrostatic stress can be a driving force for the diffusion of hydrogen, also increasing the local amount of hydrogen at the front of the notch, as illustrated in Figure 20.

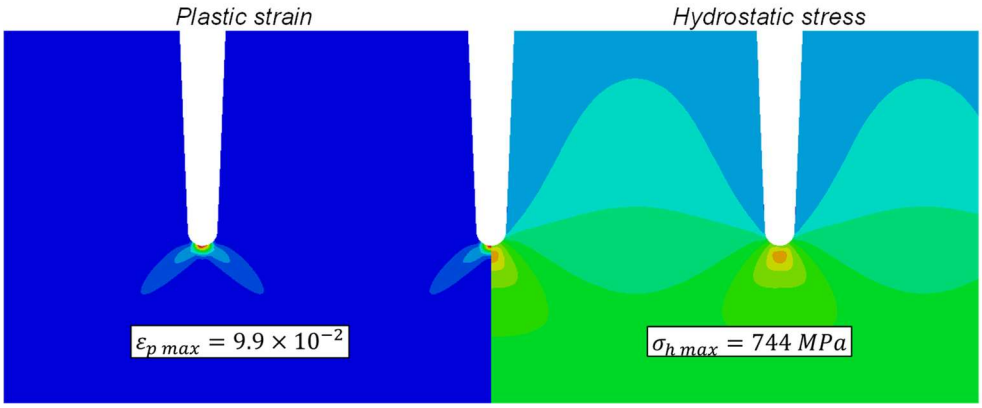


Figure 20: Numerical calculation of (left) plastic strain (right) hydrostatic stress. L=100µm, W=10µm, D=100 µm.

Consequently, favorable conditions for hydrogen cracking could be reached at the tip of the sharp V-shape grooves. But, as shown in Figure 21, a rather tight groove distribution can strongly decrease these parameters. For distances typically observed on specimens tested in corrosive solution with H2S, in the range of 50 to 100 µm, the hydrostatic stress was in the range of 600 to 800 MPa, whereas for an isolating groove, it would be over 1000 MPa. The plastic strain also was limited, below 10%, when it reached 65% for the single groove (out of the domain of validity of the model – ductile damage should occur). Thus, a tight distribution of the grooves can also reduce the risks of hydrogen assisted cracking from the tip of the groove.

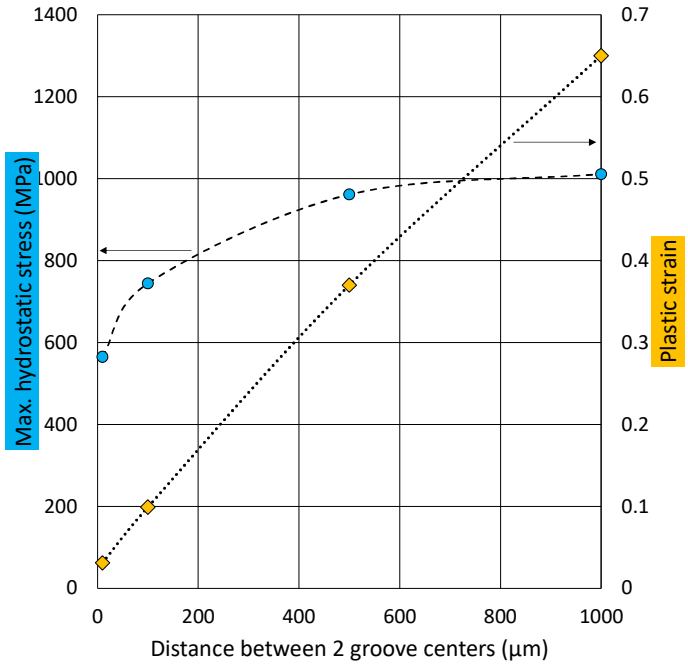


Figure 21: Evolution of the strain and hydrostatic stress at the tip of the grooves as a function of the distance for a groove depth of 100 µm.

### *4.1.2.* INFLUENCE OF THE MECHANICAL PROPERTIES

To evaluate the impact from the mechanical properties of the two steels investigated in this study, excluding any effect from the microstructure, local residual stresses and so on, calculations were performed using two different mechanical properties showing the same YS but with a higher hardening rate (lower YS/UTS ratio) for the seamless steel in comparison to the TMCP seamwelded one (previously investigated). The cases of 50 and 100 µm deep grooves distributed every 100 µm (10 µm and 20 µm

wide, respectively) were considered. The maximum stress at the tip of the grooves, the maximum plastic strain and hydrostatic stresses were evaluated in each case. The results are compared in Figure 22 and Figure 23.

For a defined geometry, the decrease of the YS/UTS ratio (corresponding to an increase of the hardening rate) led to higher equivalent stress and hydrostatic stress around the groove tip. However, a slight decrease of the local plastic strain could be observed. Considering a mechanism of enhanced corrosion rate by local stress or SSC cracking phenomenon, the local mechanical conditions would be more critical for a steel showing lower YS/UTS ratio. However, the sensitivity of the steel in terms of critical local stress/strain for SSC crack initiation must be considered to evaluate the real risk of cracking. Indeed, the microstructure and the mechanical properties are strongly linked, so that a higher YS/UTS ratio could be related to a more sensitive microstructure, or the presence of local residual stresses at the scale of the grains which would affect the stress distribution. Such aspects were not covered by the modelling work.

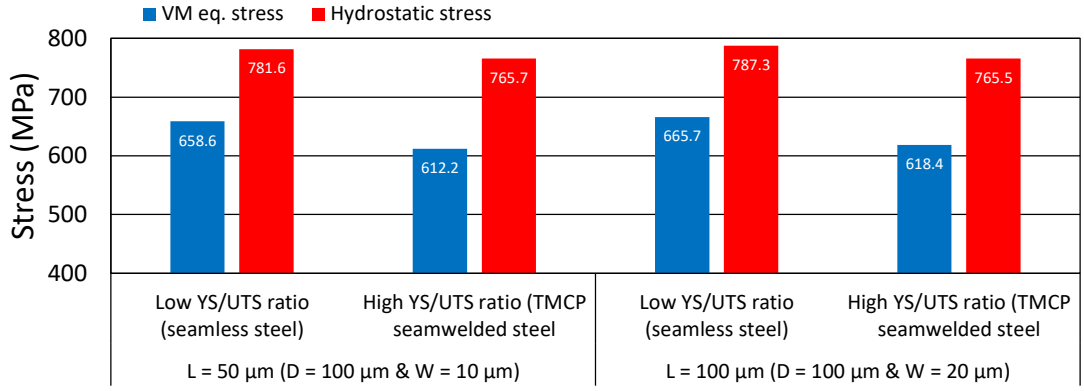


Figure 22: Maximum von Mises (VM) equivalent stress and hydrostatic stress at the tip of a groove of 50 µm and 100 µm deep, with a distribution of 100 µm and a width of 10 and 20 µm, respectively.

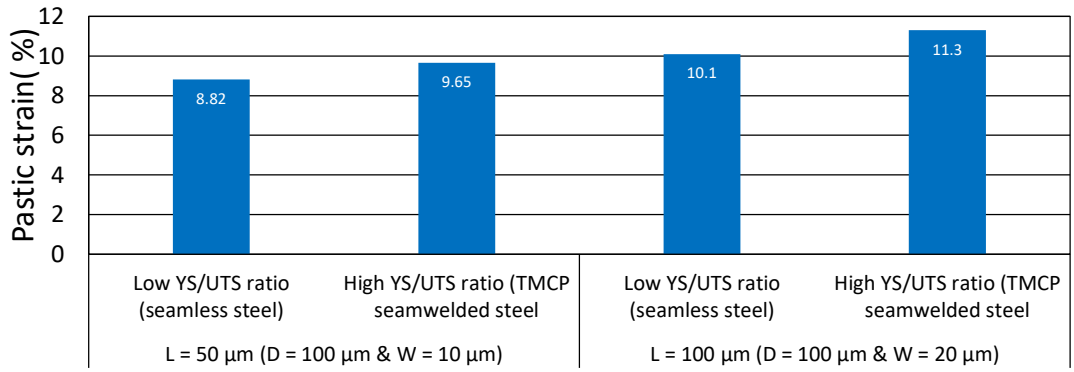


Figure 23: Maximum plastic strain at the tip of a groove of 50 µm and 100 µm deep, with a distribution of 100 µm and a width of 10 and 20 µm, respectively.

## 4.2. XRD ANALYSIS

The surface residual stress measured in the longitudinal and transversal direction on each grade and each surface finish are displayed in Figure 24. The longitudinal direction is also the one for the application of the principal stress during 4PB exposure and therefore the one we can expect having the most impact on the actual stress applied.

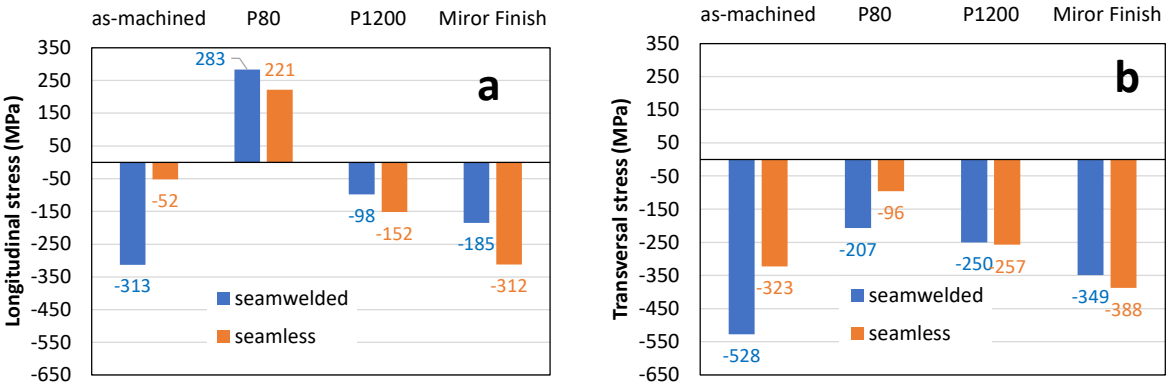


Figure 24: Effect of surface preparation on the surface residual stress. (a): measurement in the longitudinal direction – (b): measurement in the transversal direction.

One can observe that the trend is very similar for both grades although they have different microstructure. Only the actual value measured is different but only one measurement at one location was completed on both materials. In most of the cases, the residual stress is compressive reaching up to several hundreds of MPa leading therefore to a possible underestimation of the actual applied stress at the surface after loading the specimens on the 4PB jigs. Only the surface finish "P80" led to tensile residual stress leading therefore to a possible increase of the SSC test severity for this surface state.

The results of the residual stress profiles measurement are displayed in Figure 25 and Figure 26. The first figure gathers the evolution of the residual stress measured at each depth considered and the second the evolution of the FWHM giving a relative overview of the level of cold-work (the higher the FWHM, the higher the cold-work). Obviously, the residual stresses are located within the first 10 µm and almost negligible in the deeper in the bulk of the materials. Considering the expected corrosion rate in the test environment selected for the SSC tests (1 to 2 mm/year), this layer is supposed to be fully corroded within the early first days of exposure.

The same conclusion can be raised considering the superficial cold-work. The FWHM is higher at the surface of the material than in the bulk whatever the considered surface preparation. One can notice however that improving the level of surface preparation from P80 to P1200/mirror finish, i.e. below probably a threshold surface roughness, tends to decrease the superficial FWHM, i.e. the level of cold-work at the surface. These results confirmed the necessity to prepare the surface of the specimens before testing.

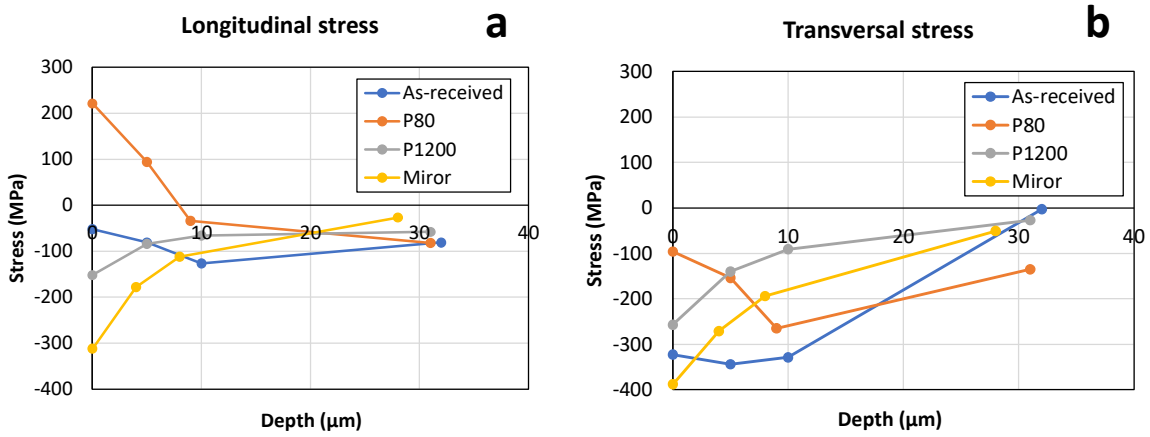


Figure 25: Effect of surface preparation on the residual stress profiles measured on the "seamless" steel grade. (a): measurement in the longitudinal direction – (b): measurement in the transversal direction.

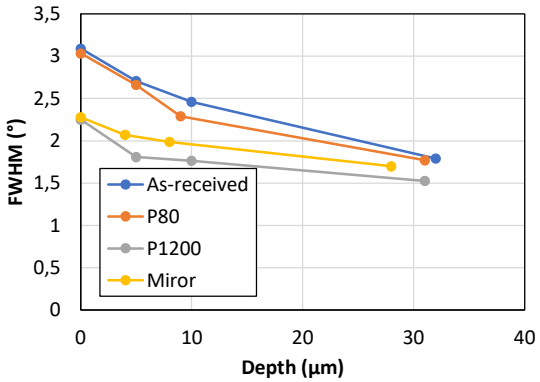


Figure 26: Effect of surface preparation on the FWHM of the diffraction peak used for the residual stress evaluation. Measurement on the "seamless" steel.

## 4.3. ROUGHNESS ANALYSIS

Roughness analyses were performed to address the quality of the different initial surface states (as-machined, P80, P1200 and mirror finish). These measurements were carried out on specimens sampled in the TMCP seamwelded pipe. Examples of the surface states are presented in the Figure 27, and roughness results are gathered in the Table 4.

The polishing was performed in the longitudinal direction to be orthogonal to the principal applied stress. Some residual polishing scratches are visible on the "mirror" surface finish, but they are not visible under naked eyes. These residual scratches are better visible under the binocular due to the surface illumination. The NACE TM0177 standard specifies a minimum average roughness (Ra) lower that 0.8 µm and all surface finish but the "P80" would therefore acceptable. Some other guidelines like EFC16 are rather specifying a minimum level of roughness of 0.2 µm that can only be achieved through refined polishing. The standard surface state used at FCI for sour qualification tests is P1200.

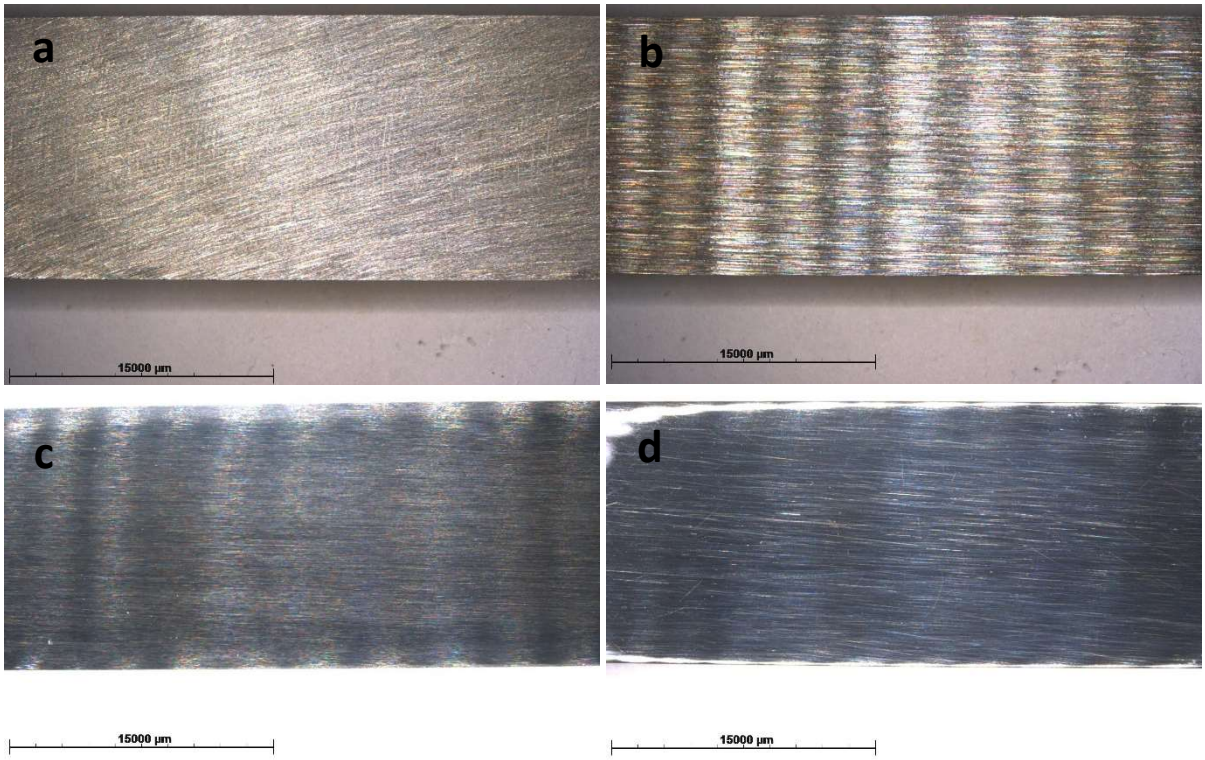


Figure 27 : Macro-observations of the initial surface after the different level of polishing considered. (a): as-machined – (b): P80 – (c): P1200 – (d): Mirror finish.

Table 4- Roughness measurements.

| State | Ra (µm) | Rq (µm) | Rz (µm) | Rt (µm) |
|---|---|---|---|---|
| **As-Machined** | 0.40±0.06 | 0.53±0.06 | 6.17±0.15 | 8.07±0.25 |
| **P80** | 2.43±0.15 | 3.07±0.15 | 23.23±1.40 | 27.23±2.03 |
| **P1200** | 0.10±0.00 | 0.10±0.00 | 2.63±0.49 | 4.33±1.81 |
| **Mirror** | 0.06±0.01 | 0.01±0.00 | 2.23±0.84 | 3.63±1.97 |

## 4.4. SSC TEST RESULTS STUDY

No failure nor crack initiation was observed after any test conditions considered, neither through macrographic observations, nor MPI. The evolution of the pH during the different tests performed to complete the program are presented in Figure 28. The standard evolution expected for a “free-pH” test is observed in each case. Indeed, the initial pH is acidic, mainly slightly below pH=3 and tends to increase during the exposure due to the alkalization of the solution through the corrosion process. The pH tends to reach a plateau after about one week of exposure that is always lower than pH=4. The pH value of the plateau varies from one test to another with an interval of about 0.3 pH unit. We also observed a decrease of pH in one test (as-received conditions in purple). This evolution is linked to a drift of the pH

probe and has no physical meaning. The final raise in pH after 700 hours of exposure occurred when the desaturation of the solution started.

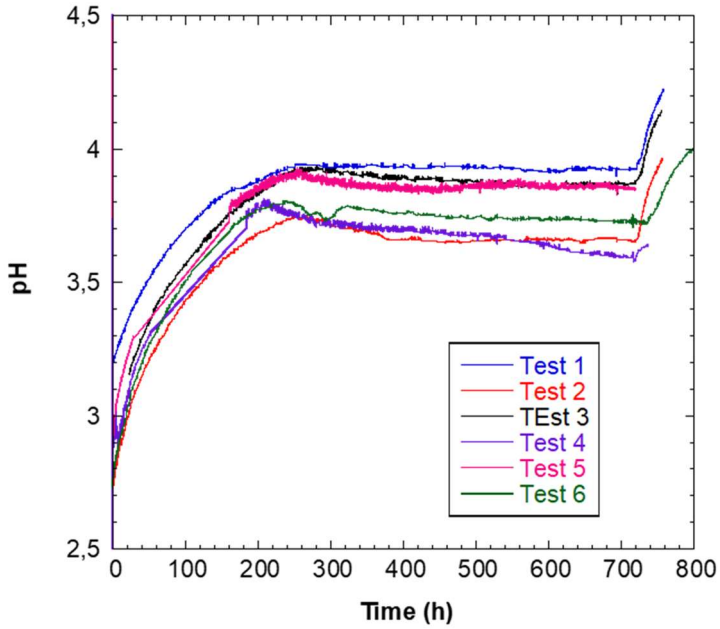


Figure 28: pH evolution during exposures.

From a qualitative point of view different macrographic states were visible after experiment as depicted in Figure 29. In a large number of cases (27 specimens out of 36 tested), the scratches inherited from the preparation route using milling appears after testing (Figure 29c-d) while not visible after the surface preparation by polishing (Figure 27). It seems that the grooves are preferentially initiating on the former milling scratches suggesting an inherit of the machining route. Note however that in such case, grooves are also initiating on the rest of the exposed surface out of the former milling scratches. The occurrence of this phenomena is not correlated with the nature of the grade or test conditions considered. In the other cases (9/36), the grooves are homogeneously distributed on the stressed surface (Figure 29a-b). The phenomenon occurs also when started from a surface polished to a mirror finish (Figure 29c)

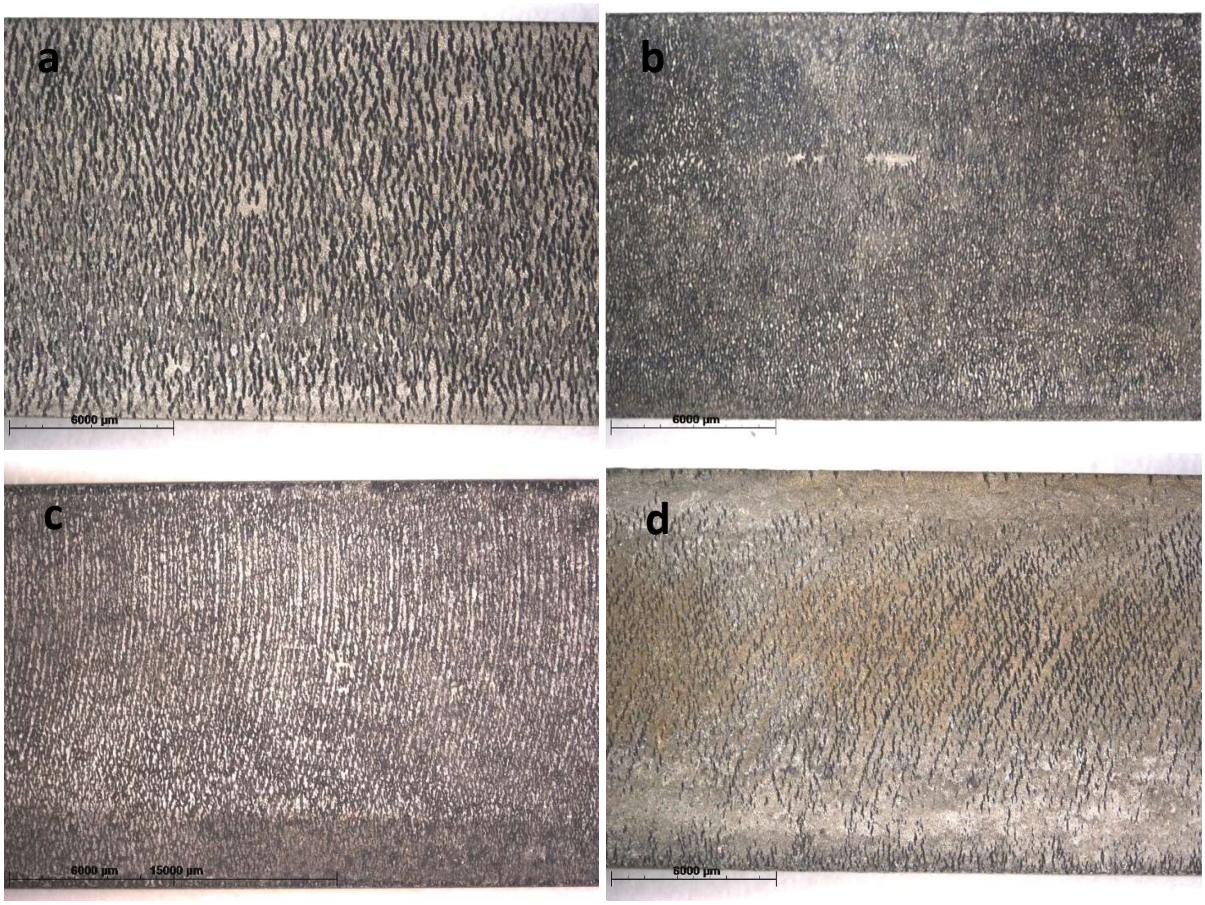


Figure 29: Typical surface of the 4PB specimens after SSC test and descaling. (a) : Seamless grade 72%AYS /P1200 – (b):seamless grade 90%AYS/P1200 – (c): TMCP – 90%AYS/Mirror finish – (d):TMCP – 80%AYS /P1200.

## 4.5. GROOVING CHARACTERIZATIONS

### *4.5.1.* EFFECT OF APPLIED STRESS

#### *4.5.1.1.* 90%AYS

Figure 30 displays the cross-sectional observations of all specimens tested under 90%AYS with the initial surface preparation "P1200". From a qualitative standpoint, the shape of the grooves forming on the specimens is clearly different for the two different grades. On the TMCP seamwelded material, the grooves have a U-shape while it is rather V-shape pattern on the seamless grade. It is also clear from the cross-section that the groove shapes and distributions seem quite homogeneous on the TMCP grade while not for the seamless. For this latter grade, it seems that the 3 specimens tested simultaneously are displaying grooves with different shapes.

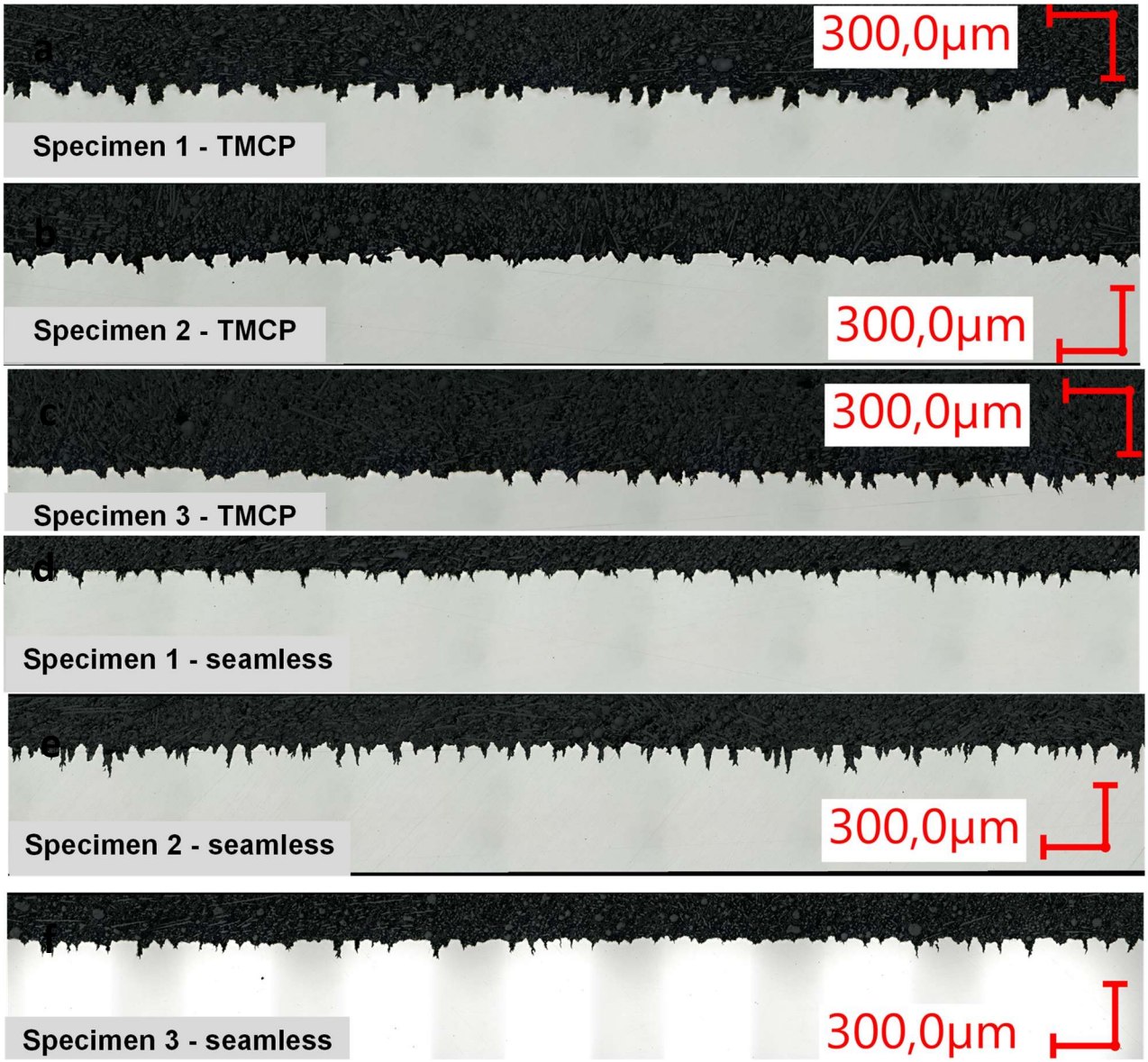


Figure 30: Metallographic cross-section of the specimens tested under 90%AYS with an initial surface finish P1200. (a-c): grade TMCP / (e-g): grade seamless.

Figure 31 shows the corresponding groove distributions which confirm the homogeneity of the grooving on the TMCP-seamwelded material with all the probability plots superimposed. On the contrary, scattering is observed between the 3 specimens sampled in the seamless pipe.

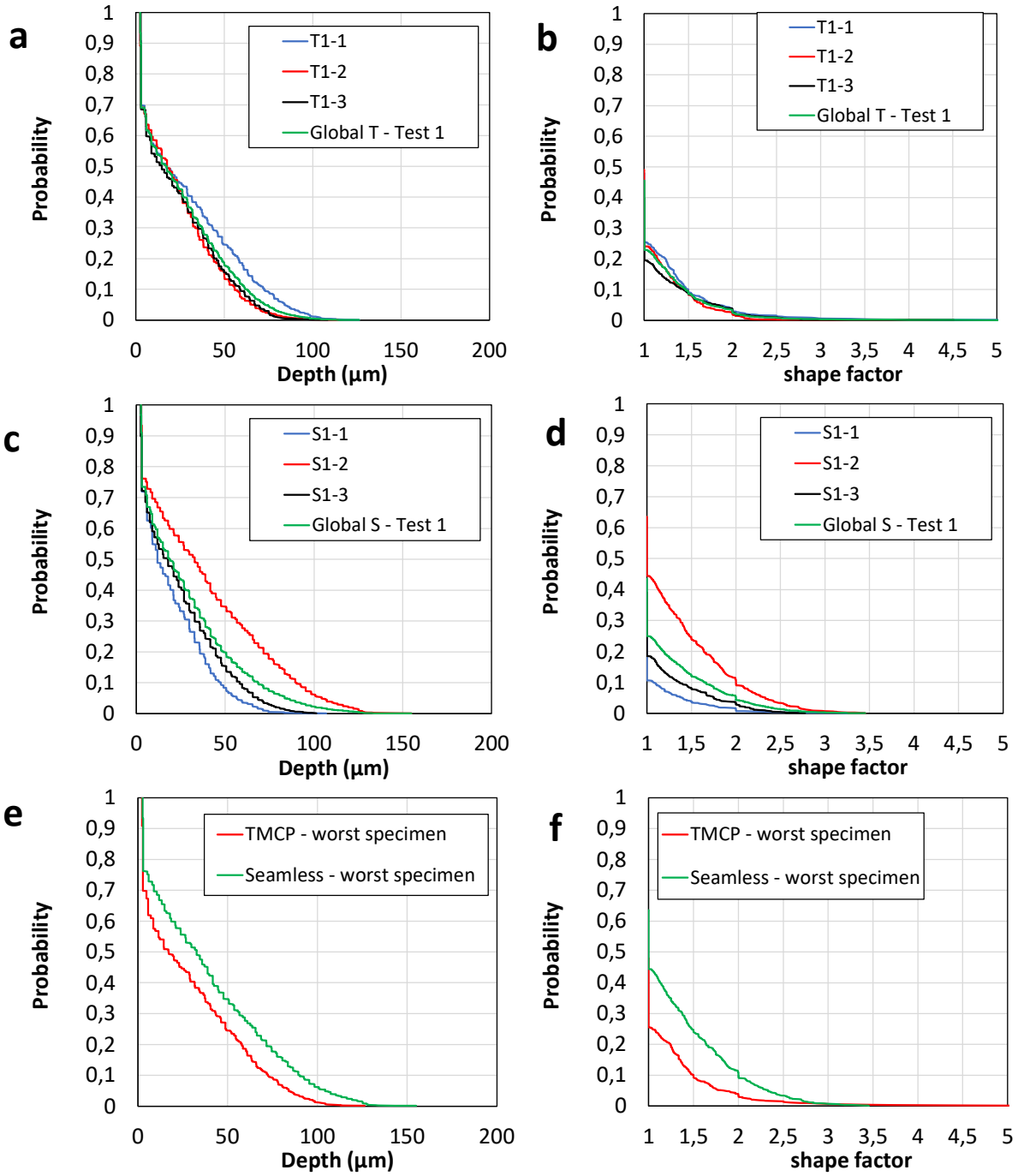


Figure 31: Groove depth and shape factor distribution of the different specimens tested under 90%AYS and an initial surface state P1200. (a-b) : TMCP seamwelded (individual measurement and average) / (c-d) : Seamless grade / (e-f) : comparison of the worst specimen of both grades.

Both grades only evidence a small fraction of grooves (< 5%) deeper than the 100 µm limit specified in EFC16 guidelines. All grooves but one in the TMCP material out of more than 800 measurements have a shape factor higher than "4" considered as the critical limit in guidelines proposed elsewhere qq2].

The difference between both materials can only be highlighted in the distribution plot when the worst specimens are compared (Figure 31e-f). When the average measurements of the 3 specimens of each material are compared, the curves are perfectly superimposed (Figure 32).

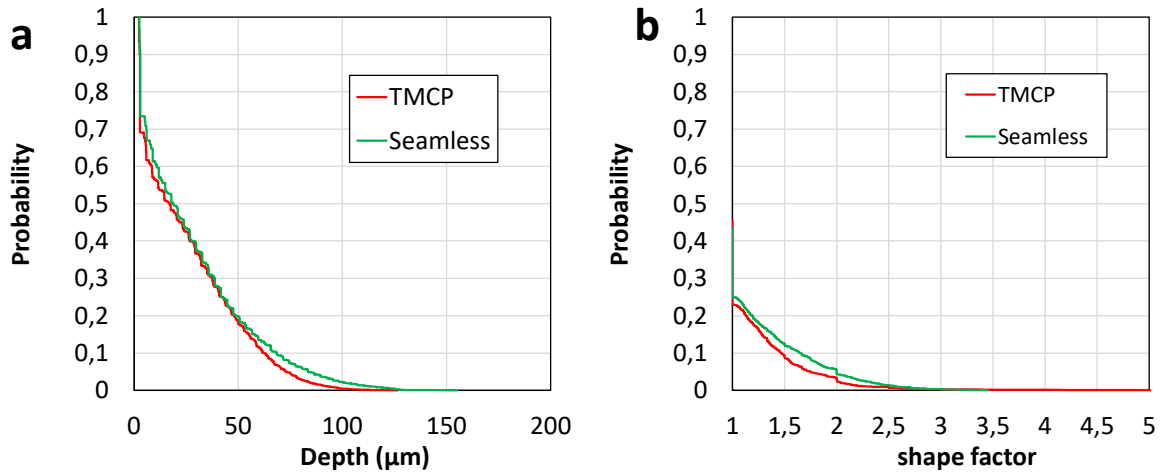


Figure 32: Groove depth and shape factor distribution of the different specimens tested under 90%AYS. Comparison of the average values considering all measurements in 3 specimens per grade (2600 to 2800 measurements per grade).

#### *4.5.1.2.* 80%AYS

Figure 33 displays the typical groove shapes observed on both grades and the associated distributions measured through image analysis. Under this stress level, both grades highlight U-shape grooves, but it seems that the grooves in the seamless pipe are turning to a V-shape at different locations (Figure 33b). From a statistical point of view, the measurements in the 3 specimens of both grades are homogeneous and there is not significant difference between the average values of both grades (Comparison not shown but the plots corresponding to the average measurements in both grades are perfectly superimpose). The difference between both grades is only the trend to see locally a transition between a U-shape and a V-shape in the microgrooving of the seamless that is not visible in the TMCP.

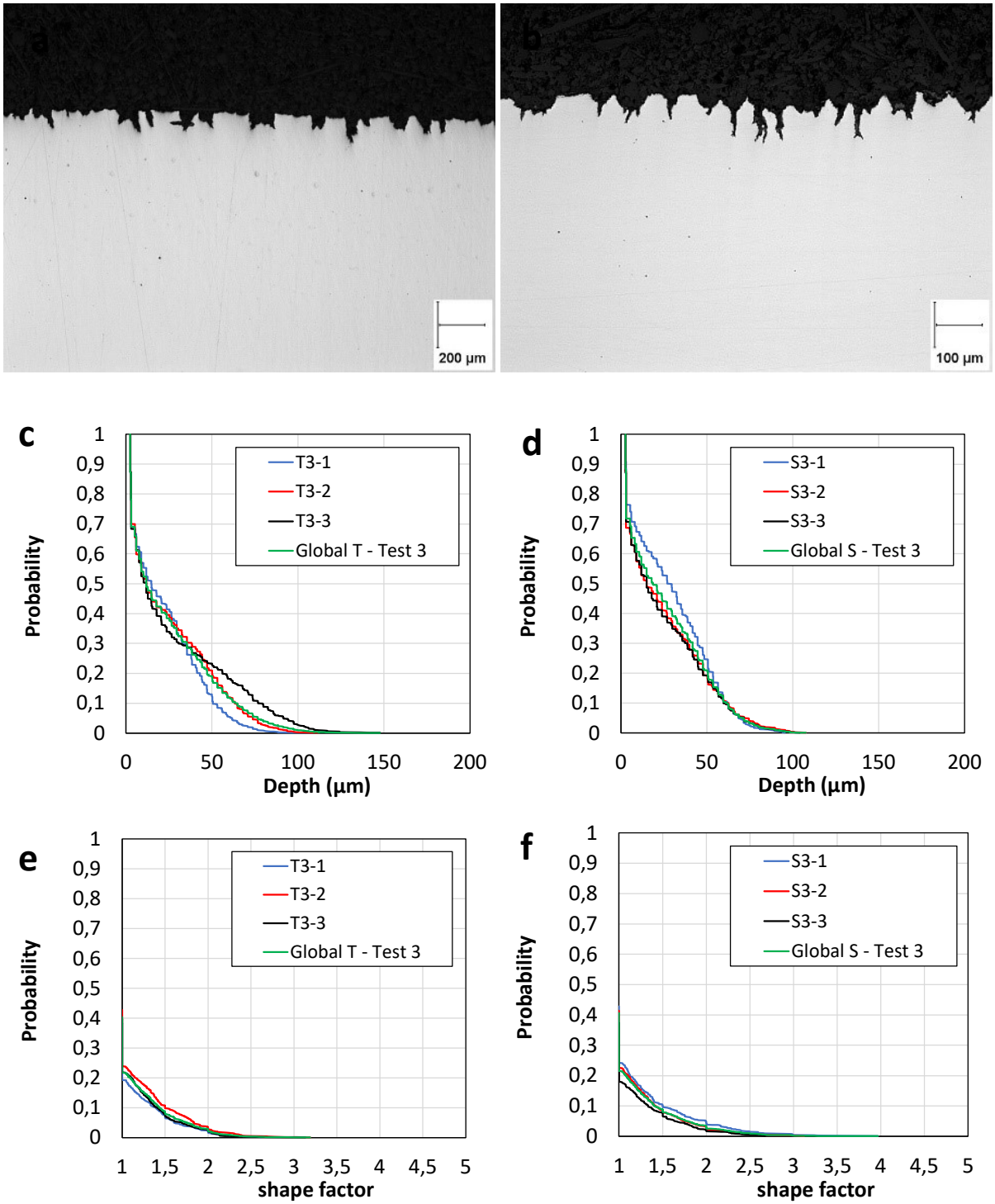


Figure 33: Typical groove shape observed in the TMCP-seamwelded grade under 80%AYS (a) and in the seamless one (b). Corresponding groove distribution for TMCP (c-e) and seamweld (d-f).

### *4.5.1.3.* 72%AYS

Under 72%AYS, grooves are visible after test on both grades underlining that the threshold stress triggering the groove formation is lower than this value for both grades. However, some differences can be locally highlighted. Mainly and as already visible under 80%AYS, some V-shaped grooves are locally visible in the seamless grade (Figure 34b) in a microgroove distribution having general U-shapes along the stressed surface of the specimens (Figure 34a). There is therefore again a trend of this grade, even under low applied stress, to form V-shaped grooves. The phenomenon is not highlighted in the TMCP-seamwelded grade. On the latter, the distribution of the grooves along the exposed surfaces is not homogeneous. Grooves are formed in some area (Figure 35a) but not or is limited in others (Figure 35b). This heterogeneity explains the large difference in the groove distribution of the 3 specimens of this grade. It also suggests that the threshold stress for groove initiation is higher in the TMCP-seamwelded grade than in the Seamless and maybe that an applied stress of 72%AYS is borderline for the TMCP. Testing under a lower stress would be needed to confirm this assumption but the fact that the grooves have not formed on the whole stressed surface for one specimen surface of this material tends to corroborate the assumption (Figure 36).

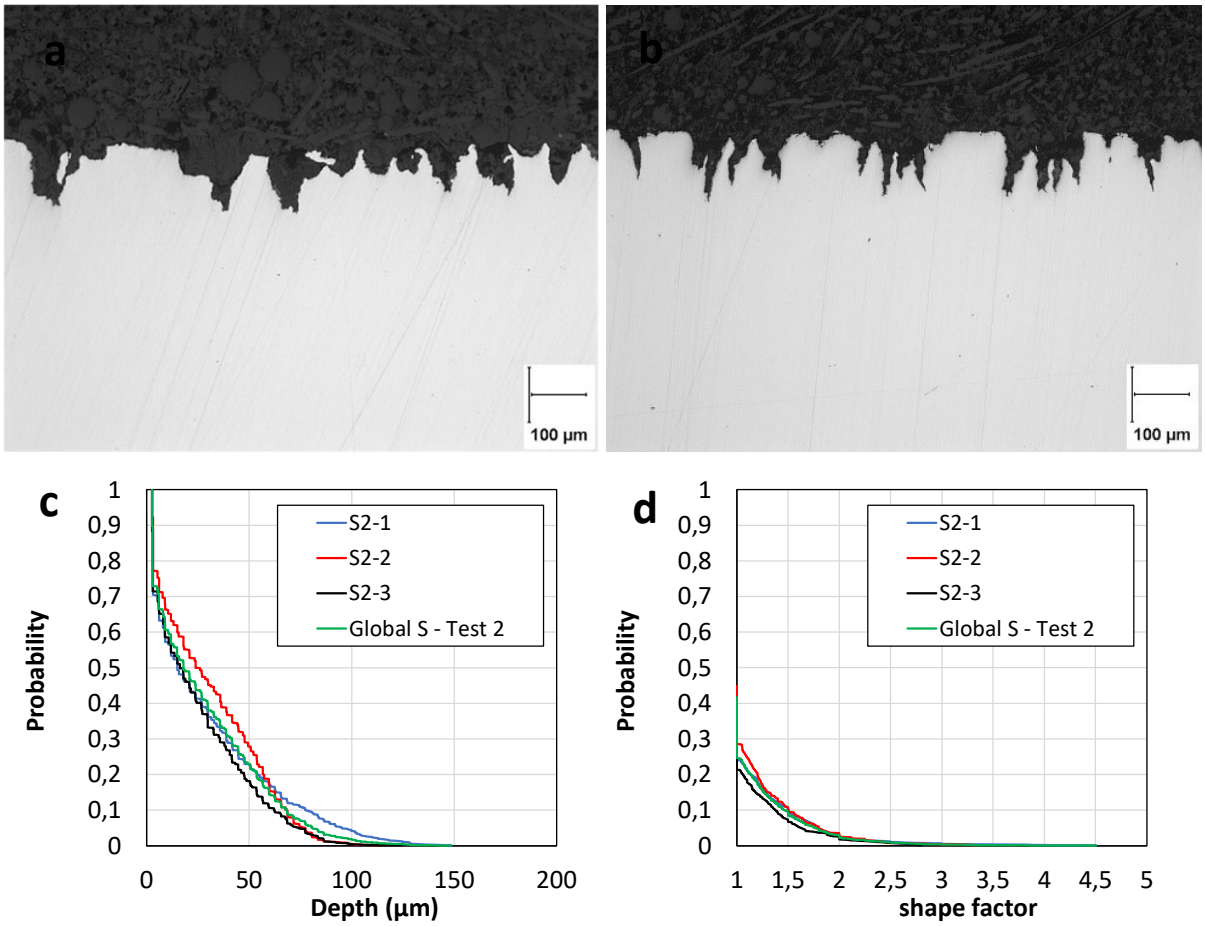


Figure 34: Typical groove shape observed in the seamless grade under 72%AYS (a) and local difference in some area (b). Corresponding statistical distribution of the grooves (c-d).

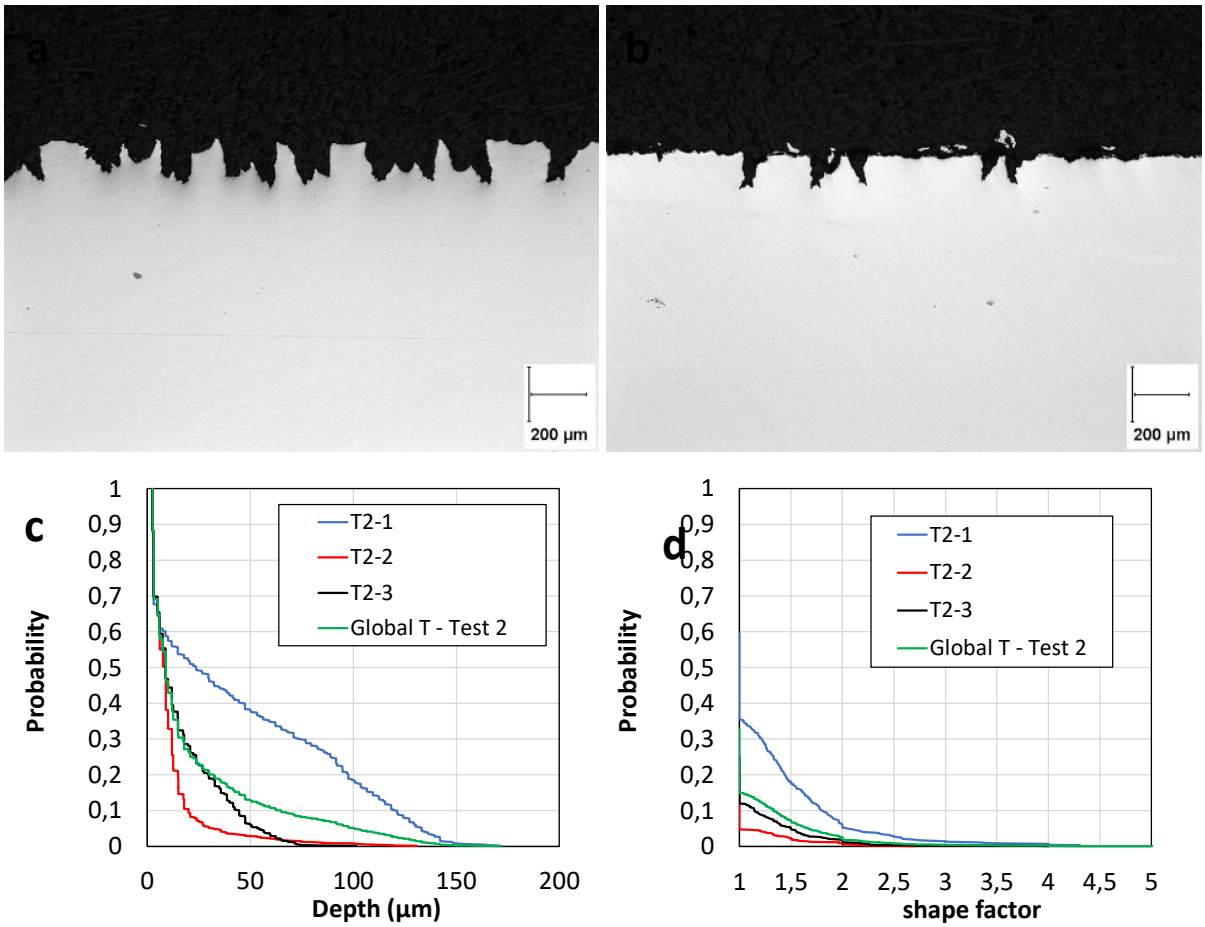


Figure 35: Typical groove shape observed in the TMCP-seamwelded grade under 72%AYS (a-b) showing heterogeneous distribution of the groove along the stressed surface. Corresponding statistical distribution of the grooves (c-d).

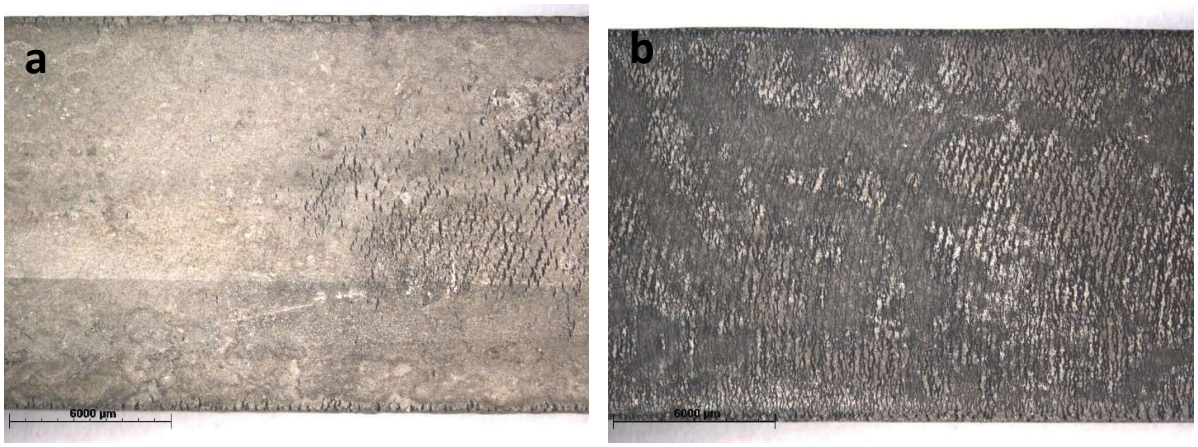


Figure 36: Macrographic observation of the stressed surface of one "TMCP" specimen (a) and one "Seamless"(b) after test under 72%AYS.

### *4.5.1.4.* ANALYSIS AND CONCLUSIONS ON THE EFFECT OF STRESS

All the results obtained in the investigations of the effect of applied stress on microgrooving are given in Figure 37 and Figure 38. First, there is obviously no significant difference between the average measurements in both grades (Figure 38a-b). Second, some differences are highlighted in the distributions of the TMCP-seamwelded material (Figure 37a-b) but that can be explained by the non-homogeneous distribution of the microgrooves on the specimens loaded at 72%AYS. On the contrary, the distributions are superimposed for the Seamless grade (Figure 37c-d). From these results, it can be concluded that, for an applied stress sufficiently higher than the one triggering the microgrooving process, no effect of the actual load can be observed. The main effect of stress observed in this work is the trend of the Seamless grade to develop V-shape grooves for high applied stress while the TMCP-seamwelded only produce U-shape patterns.

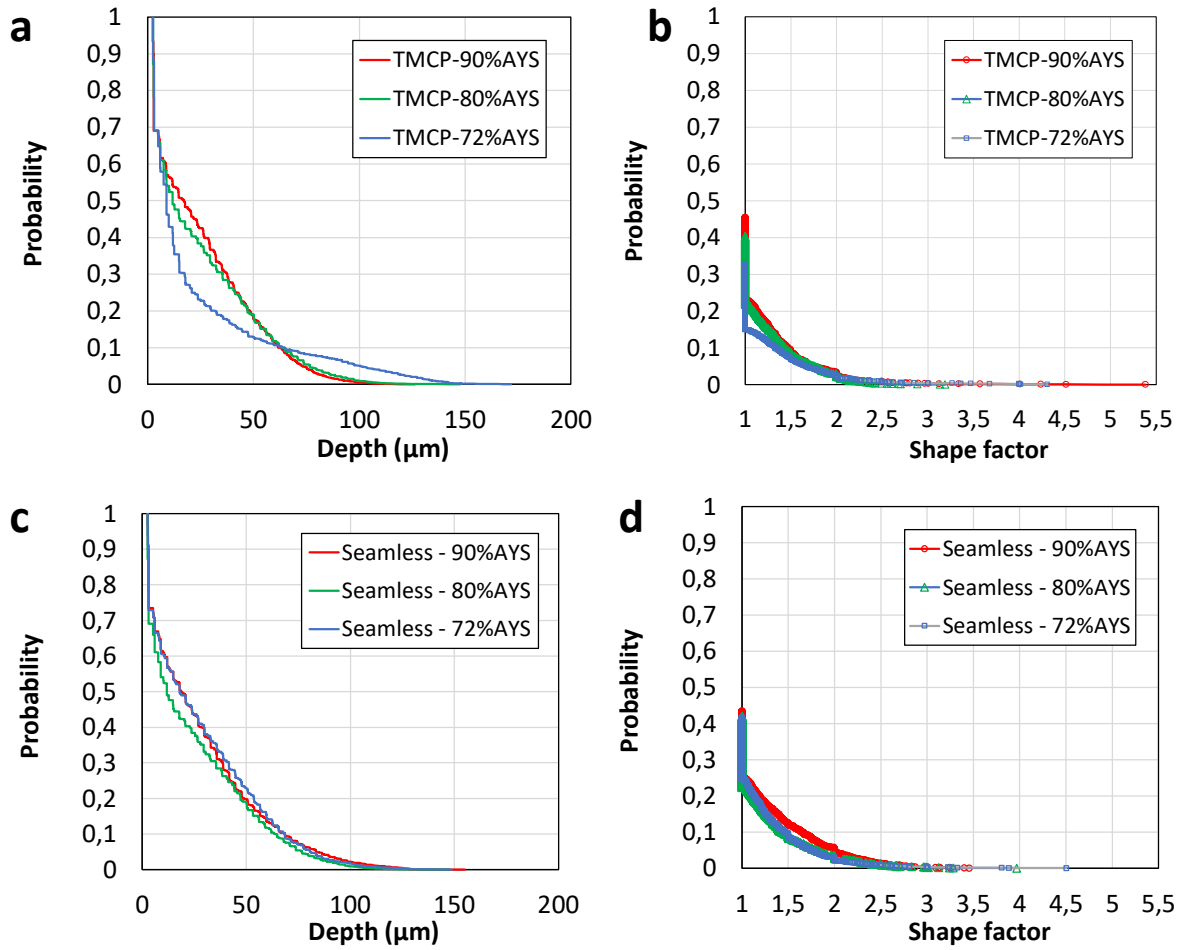


Figure 37: Effect of applied stress on grooving in both grades. (a-b) : average distributions obtained for each stress on the TMCP grade. (c-d) : average distribution for the seamless grade.

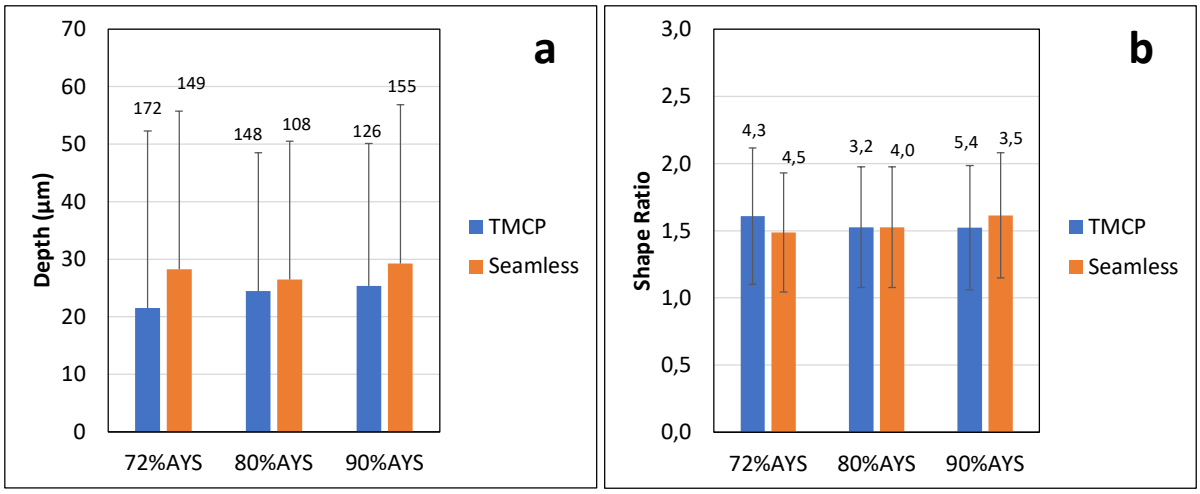


Figure 38: Effect of applied stress on grooving in both grades: average values of (a) the depths and (b) shape factor out of more than 2000 measurements per grade (the number/error bars on each histogram is the max value measured).

### *4.5.2.* EFFECT OF SURFACE STATE

The second task of the project was the evaluation of the effect of surface preparation on the development of microgrooves on both grade during sour testing under 90%AYS. The Figure 39 and Figure 41 are showing the micrographic observations after testing for TMCP seamwelded and seamless steels, respectively. From a qualitative standpoint, it is obvious that the surface preparation has no effect on the microgrooves formed on the TMCP material (Figure 39). The grooves seem quite similar whatever the initial surface. On the contrary, the polishing has clearly a beneficial effect in diminishing the grooving effect on the seamless grade. Mainly, the groove formation is very limited when starting from a surface polished to a mirror finish (Figure 41).

This trend is also confirmed in the analysis of the groove distributions on both grades. The profiles are superimposed for the TMCP material whatever the initial surface considered (Figure 40) while they become shallower and flatter with the seamless material as the initial surface quality is improved. Mainly, with the mirror finish, no groove deeper than 100 µm or with a shape factor higher than 4 can be highlighted on the contrary to other surface states (Figure 42).

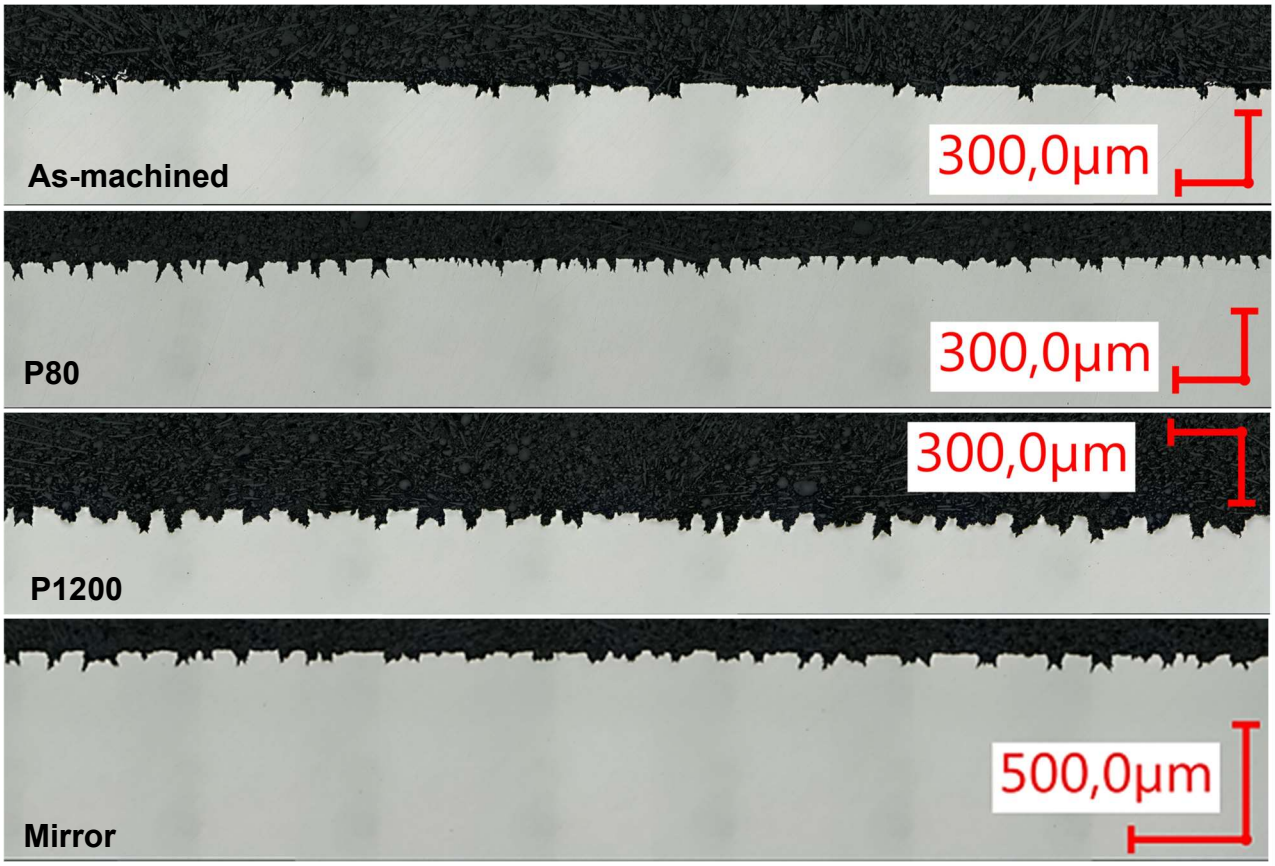


Figure 39: Micrographic observation of the grooves formed on the TMCP-seamwelded specimens after test under 90%AYS and different initial surface finish.

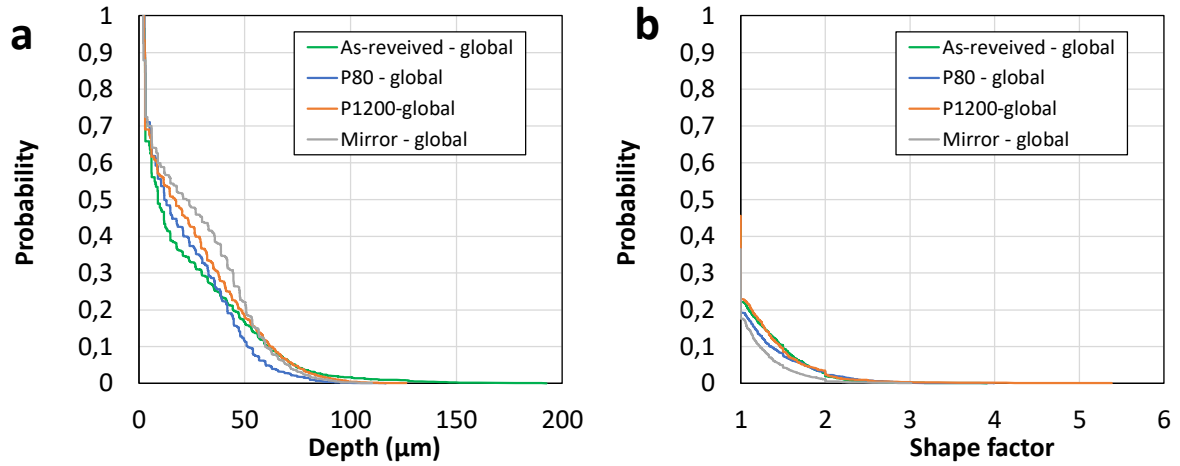


Figure 40: Groove distribution for the different initial surface state considered, measured in the TMCP specimens. (a) : groove depths / (b) : shape factor.

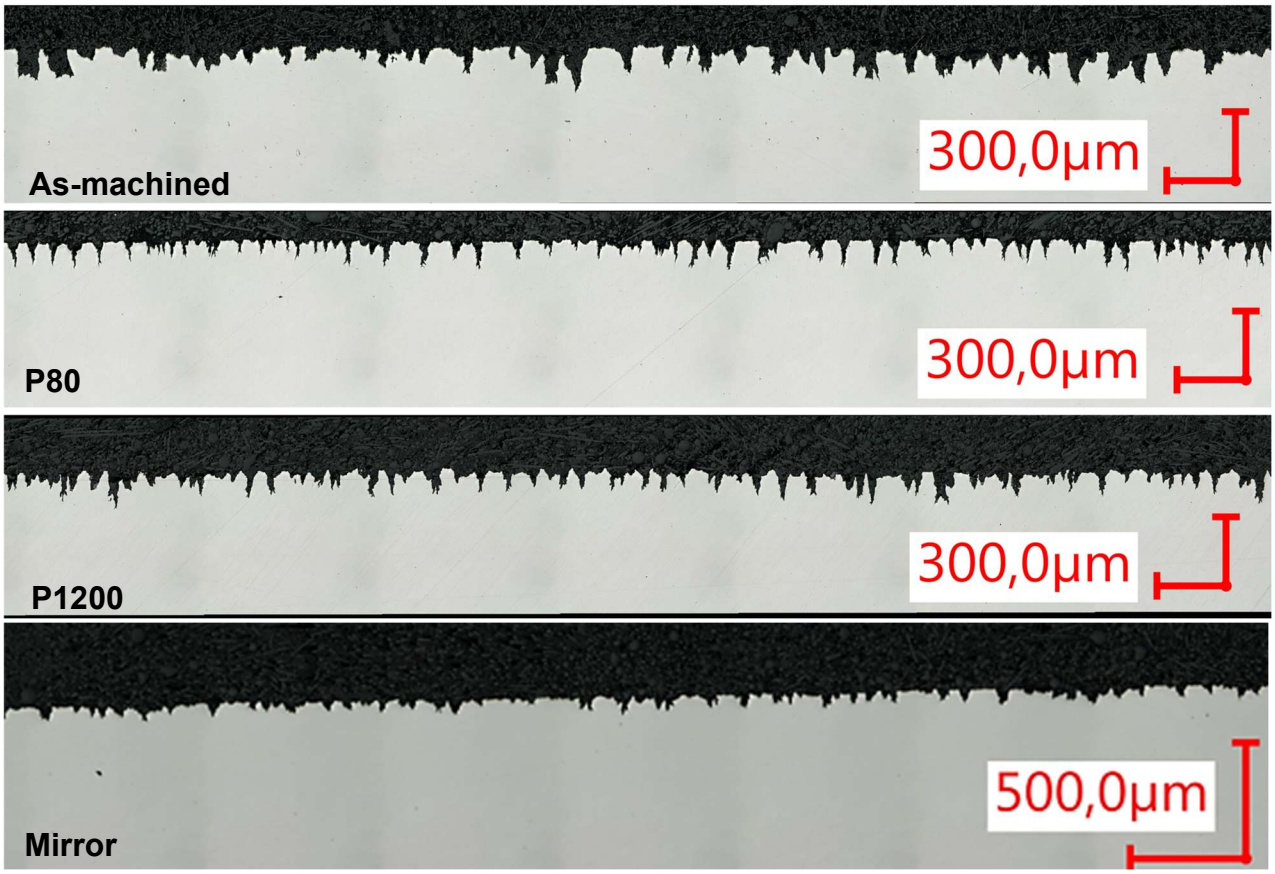


Figure 41: Micrographic observation of the grooves formed on the seamless specimens after test under 90%AYS and different initial surface finish.

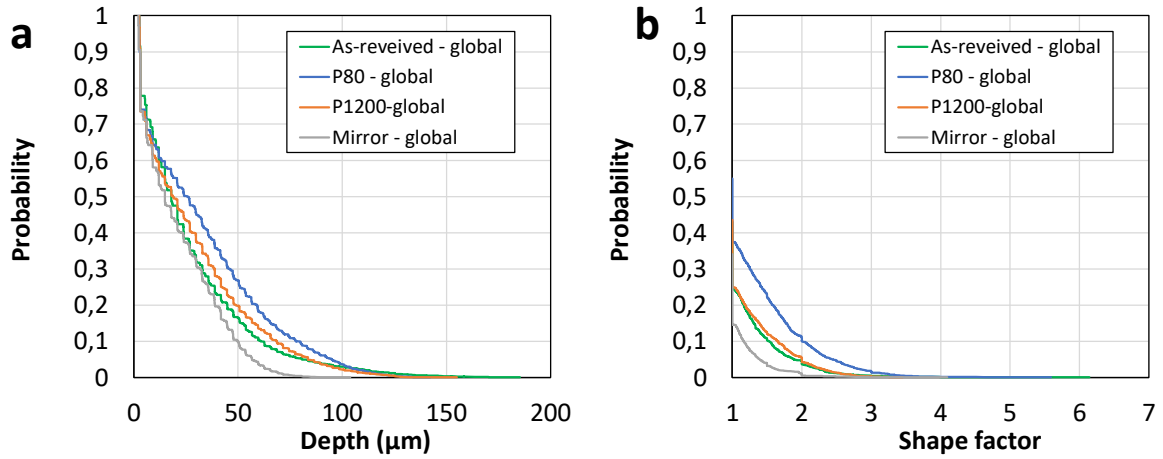


Figure 42: Groove distribution for the different initial surface state considered, measured in the seamless specimens. (a) : groove depths / (b) : shape factor.

# 5. DISCUSSION

At all investigated applied stresses, micro-grooves were obtained whereas selected X65 steels should be qualified for sour service considering their hardness (according to ISO 15156). In particular, at the lowest applied load of 72%AYS, the phenomenon of SSC should not occur, so that groove initiation by SSC mechanism may be excluded. For most of the specimens, grooves initiated at the location of former machining marks, visually removed by further mechanical grinding and polishing. Thus, it could be assumed that the local residual stress played a great role on groove formation, linked to a mechanism of enhanced dissolution by local strain and stress.

For the seamless steel, a clear impact from the surface preparation could be highlighted. On the contrary, the TMCP seamwelded was less sensitive to the initial surface state in terms of grooves depth and shape ratio. Considering the residual stresses at the surface measured by X-ray diffraction, no clear difference could be highlighted between the two steels. However, it should be pointed out the technique gave an average value over the investigated surface, with limited lateral resolution. So that local variations might not be observed. The affected depth was also limited, in the range of 10 to 30 µm. Considering the expected corrosion rate in the test environment selected for the SSC tests (1 to 2 mm/year), this layer is supposed to be fully corroded within the early first days of exposure. Thus, the difference between the two steels could be related to the microstructure, leading to different local stress and strain distribution at the scale of the grains and affecting finally groove shapes. Another explanation could be that another method with higher lateral resolution would be necessary to investigate the distribution of compressive and tensile residual stresses at the surface of the specimens.

The presence of deep and sharp grooves could be favorable for the initiation of SSC crack at the tip of the grooves due to stress concentration effect. From the modelling work, it could be highlighted that a strong interaction occurred between the stress fields around grooves. This way, a stress relaxation was obtained when the distance between grooves was lower than 300 µm, which seems to be systematically the case for the investigated steels. The conditions for crack initiation at the tip of the grooves were made unfavorable for close-packed grooves distribution. The main geometrical parameters were the depth and the distance between the grooves. The groove radius should be also an important parameter that was not investigated.

From a pure mechanical aspect, the mechanical properties of the steel can also impact the stress concentration at the groove tip. Indeed, for higher hardening rate (lower YS/UTS ratio) the local stress and hydrostatic stress are increased, and the plastic strain slightly decreased. For a mechanism of corrosion enhanced by local stress or even corrosion enhanced by local hydrogen content, that is increased with the level of hydrostatic stress, a low YS/UTS ratio could make groove growth easier in the direction of the maximum stress, this is to say from the groove tip, keeping the V-shape of the groove. On the contrary, decreasing the stress concentration could favored U-shape grooves for which the stress distribution would be drastically modified.

This assumption are also corroborated by the average corrosion rate calculated through weight loss of the 4PB specimens after testing and descaling. As highlighted by the Figure 43, the average corrosion rates measured on the 3 specimens after each test is slightly higher with the seamless grade which is quite well correlated with the deeper grooves observed in this grade. This result suggests again that grooving is a stress-assisted corrosion mechanism.

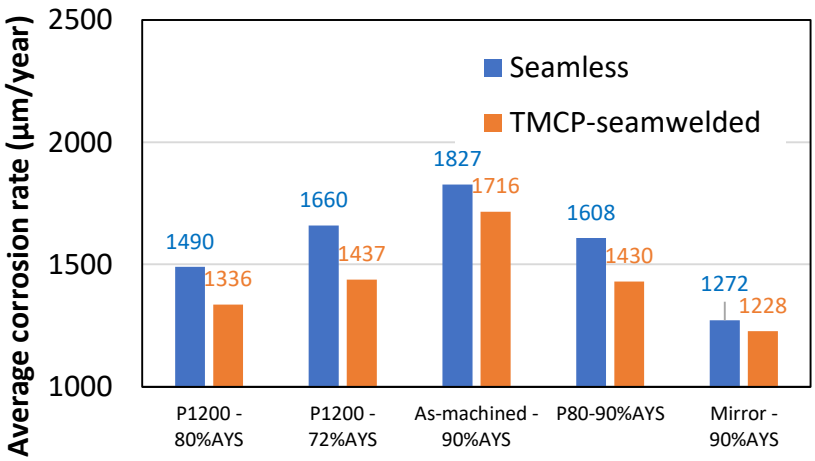


Figure 43: Average corrosion rates measured through weight loss evaluation of the 4PB specimens after SSC tests

Such observation is supported by the average groove depth measurements, presented in Figure 38, with deeper grooves for the seamless steel at all investigated applied loads compared to the TMCP steel, thus probably related to a higher corrosion rate from the tip of the groove for the seamless steel. However, the impact from the microstructure or the texture (preferential crystallographic orientations) cannot be totally excluded.

Considering now the risk of SSC from the groove tip, increased stress concentration would be also favorable for crack initiation and growth. However, the mechanical properties, particularly the YS/UTS ratio, is strongly related to the microstructure and residual stress state in the material. Thus, the inherent sensitivity of the steel could be also different, in terms for instance of critical local stress or strain. As a result, enhanced or decreased sensitivity for lower YS/UTS cannot be concluded from the current study, but stress distribution and concentration would definitely play a key role.

## 6. CONCLUSIONS

Two different X65 grades were selected for the study: TMCP seamwelded steel supplied by Liberty Steel and seamless steel supplied by Vallourec. The two steels showed similar YS and hardness, but slightly higher UTS for the seamless steel, inducing lower YS/UTS ratio. The steels were submitted to SSC tests as per NACE TM0177, using solution A and 4-point bending (4PB) loading as per NACE TM0316 at 3 different levels (72, 80 and 90%AYS). After testing, the samples were systematically inspected on cross-section using a statistical approach to evaluate groove depth and shape factor (ratio depth over width) distributions along the sample. In parallel, a numerical modelling approach was developed to evaluate the stress concentration at the tip of the grooves. The stress and strain fields were calculated as a function of geometrical parameters of the grooves and their distribution over the surface. The mechanical properties of the two different steels were also considered. The results from the experimental and modelling works were compared to identify the critical factors that could influence groove growth or initiation of SSC crack at the tip of the grooves. From the results, the following conclusions could be drawn:

- At the end of the SSC tests, no failure or crack initiation was observed for both steels at all investigated applied loads
- Grooving was observed on the tested specimens, initiating in a large number of the cases at the location of former machining marks, even if they were no more visible before the exposures after grinding or polishing of the samples. That could indicate a strong influence from plastic deformation or residual stresses.
- From the statistical characterization of the grooves, only a small difference was observed between the two steels, with slightly shorter grooves for TMCP seamwelded steel compared to the seamless steel.
- The grooves formed on TMCP steel where closer to U-shape, whereas the seamless steel showed a tendency to form V-shape grooves.
- The influence of the applied stress was rather limited, keeping statistically almost the same depth and shape factor distributions, except in the case of the lowest applied load (72%AYS) for the TMCP steel that was only partially covered with grooves, limiting the statistics of the result.
- The TMCP steel did not show clear differences in terms of groove depth and shape factor for the different surface states investigated.
- On the contrary, for the seamless steel specimens after grinding with P80 paper, both depth and shape factor were higher than for other tested conditions. With mirror polishing, the depth was particularly low and shape ratio clearly smaller.
- The residual stress measurements did not show clear difference between the steels. Moreover, the residual stress extent into the bulk was limited to the first 10 or 30 µm.
- Grinding with P80 paper was the only condition that led to tensile residual stresses, for both steels.
- No clear link could be built between surface preparation and residual stresses, probably linked to the lack of lateral resolution of the technique. However, the affected layer would be rapidly consumed by corrosion, limiting probably the impact of surface preparation for long term experiments, even if the impact on damage initiation cannot be neglected.
- The numerical calculations showed a strong stress concentration at the tip of the grooves.
- A clear interaction of the stress fields around the groove tips was observed, leading to stress relaxation phenomenon when the groove distance was below 300 µm, which was systematically observed after SSC test on the two steels.
- The levels of stress, plastic strain and hydrostatic stress were mainly controlled by the groove distance and depth. An additional geometrical factor, the groove radius, was not investigated but should also strongly influence the stress/strain fields.
- Modifying the distance between grooves would modify the stress concentration at groove tip and the possible risk of SSC initiation.
- For the two different materials, showing two different hardening rates (linked to YS/UTS ratio), it was highlighted that the stress concentration and the maximum hydrostatic stress close to the groove tip were affected.
- Considering a mechanism of stress assisted corrosion enhanced by the presence of hydrogen (corroborated by average corrosion rates measurements.), the local corrosion rate at the tip of the groove could be enhanced for steels with lower YS/UTS ratio, showing both higher maximum stress concentration and maximum hydrostatic stress, related to hydrogen concentration.
- Under such condition of higher local stress, the V-shape of the groove would be favored. However, other parameters, in particular the microstructure and its texture, could also explain the observed differences between the two steels.

To summarize, the presence of micro-grooving was systematically observed under the investigated conditions, but without clear evidence of cracking, even if a risk of SSC from the grooves was identified due to the high stress concentration which is function of depth and distribution of the grooves. The roughness and the surface residual stresses seemed to affect the groove formation, in particular former machining marks. The applied stress showed minor impact on groove aspect in the investigated range, which is an additional argument supporting that grooving is not SSC but rather stress-assisted corrosion.

Further investigations of the impact of local microstructure and stresses should be performed to obtain further insight on the mechanism of groove formation and growth and risks of SSC from the groove tip. For the qualification of the severity of the grooves, another parameter, the groove tip radius should also be included, as potentially strongly influencing the local stress distribution around the groove.

## 7. REFERENCES


[1] R. J. Pargeter, "The effect of low H2S concentration on welded steels" NACE Corrosion Conference 2000, paper 00143

[2] T. Anderson, W. Huang, G. Wadsworth, H. Jo Jun, D. Fairchild, T. Neeraj, A. Ozekcin, NACE Corrosion Conference 2020 – paper 14845 – issued without communication due to the covid crisis.

[3]J. L. Crolet "Analysis of the various processes downstream cathodic hydrogen charging IV: detailed mechanism of sulphide stress cracking" Materiaux & Techniques 104 (303) (2016).14 p.

[4] J. L. Crolet "Analysis of the various processes downstream cathodic hydrogen charging: Mechanistic issues on charging, degassing and sulphide stress cracking" Materiaux & Techniques 104 (302) (2016) 15 p.

[5] T. Haase, C. Kalwa, C. Bosch, "Systematic investigation of the role of stress-induced pits and grooves in SSC 4PB testing of line pipe steel" NACE Corrosion Conference 2021, paper 16571.

[6] C. Mendibide, C. Duret-Thual, "Formation of Microgrooving on C110 Casing Steel After Sulfide Stress Cracking Test" Corrosion (2021) 77 (4) pp. 434-444.

[7] V. Smanio, M. Fregonese, J. Kittel, T. Cassagne, F. Ropital, B. Normand "Contribution of acoustic emission to the understanding of sulfide stress cracking of low alloy steels", Corrosion Science 53 (2011) pp. 3942-3949

[8] V. Smanio, "Etude des mécanismes de fragilisation par l'hydrogène des aciers non allies en milieu H2S humide : contribution de l'émission accoustique" translation : 'Study of the hydrogen embrittlement mechanisms of non-alloyed steels in wet H2S media : contribution of the acoustic emission technique" PhD thesis n°2008-ISAL0129, Insa de Lyon (2008), France.

[9] C. Mendibide, H. Michaud, F. Pineau, H. Marchebois, "Role of the Machining Residual Stresses on the Sulfide Stress Cracking Resistance of Carbon Steel Evaluated According to NACE TM0177 Method A" Corrosion 68 (10) (2012) pp.897-903

[10] D. Pilkey, W. Pilkey, Peterson's Stress Concentration Factors, Wiley&Sons, 2017.

[11] G.L. de Faria, L.B. Godefroid, F.V. Nery, Damage evolution in a tensile specimen of a ductile stainless steel, Rem Rev. Esc. Minas. 69 (2016) 175–183.